Dalton Transactions

ROYAL SOCIETY OF CHEMISTRY

PAPER

View Article Online
View Journal | View Issue

Cite this: *Dalton Trans.*, 2025, **54**, 12482

Functionalized Li/NH_2/MIL-101(Cr) and Li/NH_2/MIL-100(Fe) for lithium adsorption and separation from aqueous solutions

Yanjia Zhou, Xiaodong Tang, * Jingjing Li, Dayong Qing and Hong Wang

MIL-101(Cr) and MIL-100(Fe) are both representative MIL-type Metal–Organic-Framework (MOF) materials, renowned for their large specific surface areas and size-tunable characteristics, making them suitable candidates for Li^+ extraction from lithium-containing solvents. By introducing $-NH_2$ functional groups and using $LiNO_3$ as both a template and a mineralizer, the functionalized MOF materials Li/NH_2/MIL-101(Cr) and Li/NH_2/MIL-100(Fe) were synthesized. Following modification, their Li^+ adsorption capacities were increased, reaching 43.58 and 38.22 mg g^{-1}, respectively. The dosage of mineralizer, initial Li^+ concentration, adsorbent dosage, solution pH value, and temperature all have an impact on the adsorption capacity of adsorbents. In addition, through the establishment of the pseudo-first-order kinetic model and the pseudo-second-order kinetic model, as well as Langmuir and Freundlich thermodynamic models, it was determined that the adsorption of the materials was due to monolayer chemisorption, and the adsorption process was exothermic. Furthermore, both adsorbents showed good reusability, retaining over 85% of their initial adsorption capacity after four adsorption–desorption cycles, highlighting their practical applicability in lithium recovery processes. In Mg–Li mixed solution systems, both materials exhibited exceptional Li^+ selectivity. At a low Mg^{2+}/Li^+ ratio of 3, the separation factor (α) exceeded 80; even at a high Mg^{2+}/Li^+ ratio of 10, α remained near 50. Additionally, in systems with the coexistence of multiple interfering ions, the distribution coefficient (K_d) followed the order: $Li^+ \gg Mg^{2+} > Ca^{2+} > Na^+ > K^+$. In the mixed systems, Li/NH_2/MIL-101(Cr) and Li/NH_2/MIL-100(Fe) exhibited a certain separation effect for Li^+ against competing cations.

Received 1st June 2025,
Accepted 17th July 2025

DOI: 10.1039/d5dt01288k

rsc.li/dalton

1. Introduction

Metal–Organic Frameworks (MOFs) are porous crystalline materials formed through the self-assembly of metal ions/clusters and organic ligands *via* coordination bonds. MIL-type MOFs, including MIL-101, MIL-100, MIL-53, MIL-68, and so on, exhibit distinct structural and functional properties[1,2] such as MIL-101(Cr) with a mesoporous cage structure and exceptional adsorption capacity, MIL-53(Al) with a "breathing effect" enabling dynamic responses to external stimuli, and MIL-125(Ti) with combined photocatalytic activity.[3–6] Their high surface area, tunable pore sizes, and abundant active sites make them highly promising for applications in gas storage, separation, catalysis, drug delivery, and sensing. Due to the above properties, these materials are also suitable for Li^+ extraction from liquid lithium resources. Previous studies have demonstrated that MIL-type MOFs do affect Li^+ extraction. Wei *et al.*[7] synthesized MIL-121 *via* cooling crystallization to achieve an Li^+ adsorption capacity of 0.18 mmol g^{-1} with excellent thermal stability. Huangfu *et al.*[8] prepared MIL-100(Fe) using HF and HNO_3 as mineralizers, reporting a maximum Li^+ adsorption capacity of 48.8 mg g^{-1}, and studied the detailed adsorption mechanism.

With the development of technologies such as lithium-ion batteries, the consumption of lithium is increasing day by day. Therefore, continuous research and development of products and methods for extracting Li^+ from various resources is an inevitable path for the sustainable development of related industries.[9,10] However, for the adsorption process in Li^+ extraction from solvents, the adsorption capacity is only one of the critical indicators. Realistic liquid lithium resources contain competing ions like Mg^{2+}, Na^+, K^+, and Ca^{2+}, with the separation of Mg^{2+} and Li^+ being more difficult due to their similar physicochemical properties.[11] Thus, it is necessary to improve both the adsorption capacity and the separation selectivity at the same time for Li^+ extraction adsorbents.

Southwest Petroleum University, Department of Chemistry and Chemical Engineering, Chengdu, 610500 Sichuan, China. E-mail: txda429@163.com

This study selected typical MIL-type MOFs as the research objects: the Cr-based MOF MIL-101(Cr) synthesized with terephthalic acid (H_2BDC) as the organic ligand, and the Fe-based MOF MIL-100(Fe) prepared using trimesic acid (H_3BTC) as the organic ligand. The dicarboxyl groups of H_2BDC form fewer coordination bonds with metal ions, but their linear structure enables uniform stress distribution in the framework. H_2BDC provides more coordination bonds, forming a denser coordination network with metal ions, yet this may lead to greater local stress in the framework. In addition, using Cr-based or Fe-based metal centers will result in differences in the properties of the synthesized MOFs due to the inherent property differences between the metal ions themselves. Their molecular structures are depicted in Fig. 1. MIL-101(Cr) exhibits two types of cages with sizes of 29 and 34 Å, which are interconnected through pentagonal and hexagonal windows (about 12–16 Å), featuring a spacious pore structure that enables rapid diffusion of Li^+ to internal adsorption sites. Additionally, MIL-101(Cr) displays a high specific surface area which increases surface active sites and boosts the probability of collision with adsorbates.[5] MIL-100(Fe) is characterized by a cubic unit cell with a supertetrahedral structure, comprising two types of cages with sizes of about 25 and 29 Å, which are interconnected through microporous windows of approximately 5.5–8.8 Å.[12]

To enhance the Li^+ adsorption and separation performance, $LiNO_3$ was introduced as both a template and a mineralizer. During synthesis, Li^+ from $LiNO_3$ constructs a Li^+-size-adapted microenvironment within adsorbents, thereby significantly improving their Li^+ recognition capability. Unlike conventional acidic mineralizers (*e.g.*, HF and HNO_3), $LiNO_3$, as a neutral salt, induces milder regulation of metal cluster formation kinetics and crystallization processes. This characteristic not only reduces the complexity of synthetic control but also mitigates the severe aqueous environmental contamination risks associated with HF/HNO_3 during both synthesis and post-processing stages. Furthermore, to optimize Li^+ selective adsorption, 2-aminoterephthalic acid (2-NH_2-BDC) was employed as an aminated functional organic ligand to synthesize aminated Li/NH_2/MIL-101(Cr) and Li/NH_2/MIL-100(Fe). The grafted –NH_2 groups establish weak coordination bonds with Li^+ while modulating the local charge distribution on the adsorbent surface, thereby fine-tuning electrostatic interactions for enhanced selectivity.[13]

Furthermore, adsorption kinetic and thermodynamic models were established to systematically investigate the adsorption behaviors of Li/NH_2/MIL-101(Cr) and Li/NH_2/MIL-100(Fe). The adsorption mechanisms were thoroughly analyzed *via* multi-characterization techniques, including BET surface area measurements, zeta potential analysis, FT-IR spectroscopy, and XPS. The results confirmed that both aminated MOFs exhibit not only excellent adsorption capacity but also superior Li^+ and Mg^{2+} separation performance, highlighting their potential as efficient adsorbents for Li^+ extraction from complex lithium-containing solutions.

2. Materials and methods

2.1 Materials

Chromic nitrate nonahydrate ($Cr(NO_3)_3{\cdot}9H_2O$, ≥99%) and lithium nitrate ($LiNO_3$, 99%) were obtained from Shanghai Maclin Biochemical Technology Co., Ltd. Terephthalic acid (H_2BDC, 99%), trimesic acid (H_3BTC, 98%), 2-aminoterephthalic acid (2-NH_2-BDC, >98%), and calcium chloride ($CaCl_2$, 97%) were obtained from Shanghai Aladdin Biochemical Technology Co., Ltd. Ferric nitrate nonahydrate ($Fe(NO_3)_3{\cdot}9H_2O$, AR), *N*,*N*-dimethylformamide (DMF, AR), anhydrous ethanol (CH_3CH_2OH, AR), magnesium sulfate ($MgSO_4$, AR), potassium chloride (KCl, AR), methanol (CH_3OH, AR), calcium sulfate ($CaSO_4$, AR) and sodium chloride (NaCl, GR) were obtained from Chengdu Cologne Chemicals Co., Ltd. Lithium chloride (LiCl, 99%) was obtained from Shanghai Bofei Meike Chemical Technology Co., Ltd. Magnesium chloride ($MgCl_2$, 99%) was obtained from Shanghai Bichen Biochemical Technology Co., Ltd. All the reagents above were

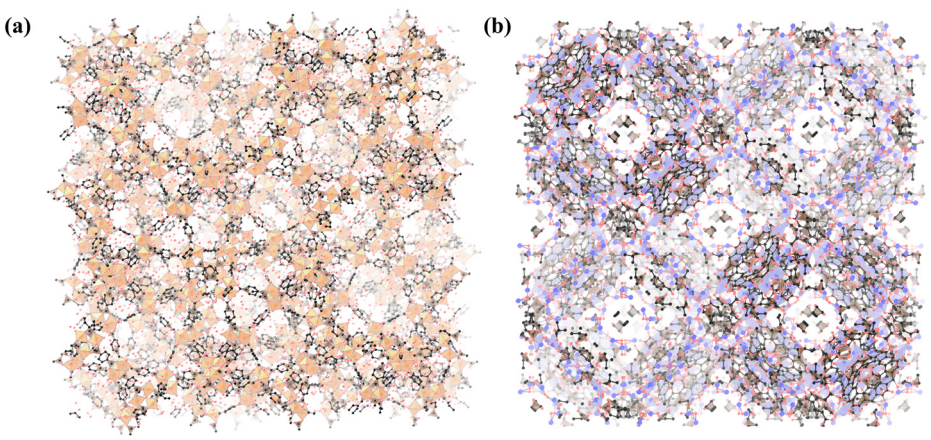

Fig. 1 Molecular structure of MIL-101(Cr) (a) and MIL-100(Fe) (b).

used as received, and deionized water was used as the water source throughout the experiment.

2.2 Preparation of Li/NH_2/MIL-101(Cr) and Li/NH_2/MIL-100(Fe)

Preparation processes of MIL-101(Cr), MIL-100(Fe), and their derivatives are shown in Fig. 2.

2.2.1 Synthesis of Li/NH_2/MIL-101(Cr). 1 mmol of Cr$(NO_3)_3{\cdot}9H_2O$, H_2BDC, and varying amounts of $LiNO_3$ (0, 0.25, 0.5, 0.75, and 1 wt%) were mixed in 5 mL of DMF. The mixture was placed in a Teflon-lined autoclave and subjected to hydrothermal crystallization at 180 °C for 8 h, followed by cooling to room temperature at a rate of 3 °C h^{-1}. After reaction completion, the product was separated by centrifugation, washed three times with DMF and anhydrous ethanol, and vacuum-dried at 120 °C to a constant weight to obtain Li/MIL-101(Cr). By replacing H_2BDC with 2-NH_2-BDC while keeping all other procedures identical, Li/NH_2/MIL-101(Cr) was synthesized.

2.2.2 Synthesis of Li/NH_2/MIL-100(Fe). 5 mmol of Fe$(NO_3)_3{\cdot}9H_2O$, 3.33 mmol of H_3BTC, and varying amounts of $LiNO_3$ (0, 0.25, 0.5, 0.75, and 1 wt%) were mixed in 5 mL of deionized water. The mixture was placed in a Teflon-lined autoclave and subjected to hydrothermal crystallization at 160 °C for 12 h, followed by cooling to room temperature at a rate of 3 °C h^{-1}. After the reaction, the product was separated by centrifugation, washed three times with deionized water and anhydrous ethanol, and vacuum-dried at 150 °C to constant weight to obtain Li/MIL-100(Fe). By replacing H_3BTC with a mixture of 3.33 mmol H_3BTC and 2-NH_2-BDC while keeping all other procedures identical, Li/NH_2/MIL-100(Fe) was synthesized.

2.3 Characterization

The X-ray diffraction (XRD) analysis was performed to investigate the phase composition and crystal structure of the samples. The measurements were conducted under the following experimental conditions: radiation source: Cu-Kα, operating voltage: 40 kV, operating current: 40 mA, scanning range: 5–90°. The structure of materials was observed by infrared (IR) spectroscopy. FT-IR spectra were collected using KBr pellets of samples on a WQF-520 FTIR (wavenumber range of 4000–400 cm^{-1}). The elemental composition and molecular structure of the materials were analyzed by X-ray photoelectron spectroscopy (XPS) on a Thermo Scientific K-Alpha. The sample chamber's pressure was maintained below 2.0×10^{-7} mbar before introducing the sample into the analysis chamber (spot size: 400 μm, operating voltage: 12 kV, filament current: 6 mA; full-scan pass energy was set to 150 eV with a step size of 1 eV, while the narrow-scan pass energy was set to 50 eV with a step size of 0.1 eV). The surface morphologies of the materials sprayed with gold pretreatment were observed by scanning electron microscopy (SEM) on a Zeiss Sigma 300 (energy spectrum: Oxford Xplore 30). The specific surface area (BET) of the composites was measured by a 3Flex Version 5.00 automatic specific surface area and porosity analyzer (the maximum degassing temperature was 300 °C, the gas for adsorption testing was N_2, and the dehydration time was 8 h). Thermogravimetric (TG) analysis was conducted to evaluate the thermal stability of the samples under a N_2 atmosphere (temperature range: 40–800 °C, heating rate: 20 °C min^{-1}, gas flow rate: 30 mL min^{-1}). Zeta potential analysis was performed to evaluate the surface charge characteristics of the samples in deionized water at different pH values (particle size range: 1–50 μm, measurement mode: potentiometric titration, error analysis: error bars represent 95% confidence level).

2.4 Adsorption experiments and relevant calculations

2.4.1 Li^+ adsorption capacity. About 20 mg of the adsorbent was completely dispersed in 10 mL of the simulated aqueous solution (except for the simulated mixture solvent

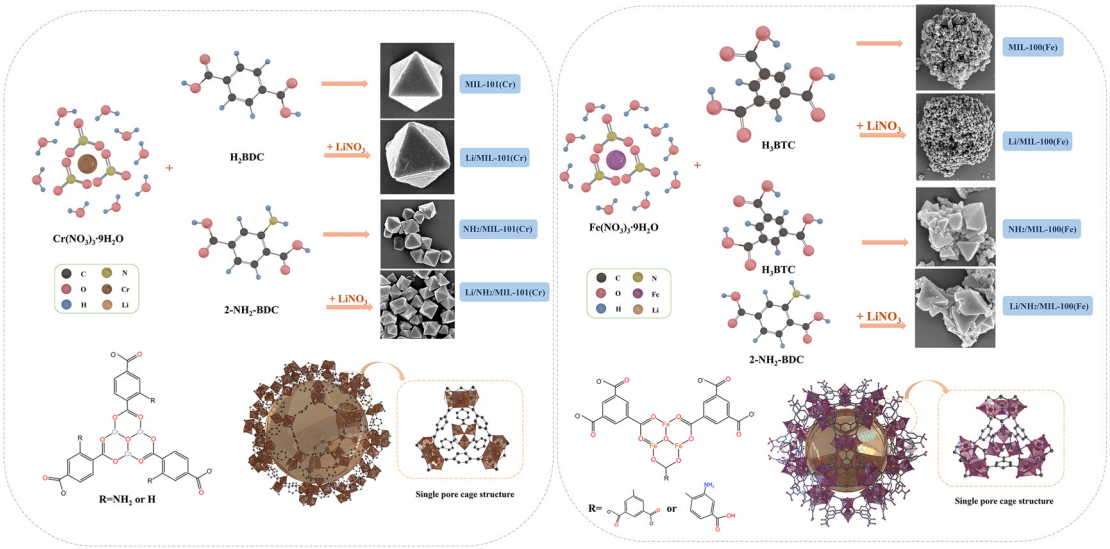

Fig. 2 Preparation processes of MIL-101(Cr), MIL-100(Fe), and their derivatives.

with multiple interfering ions, the anions in all other simulated solutions are Cl^-), and placed in a shaker for agitation at a set temperature for a specified duration. The adsorbent was then separated *via* microporous filtration, with the filtrate being collected as the post-adsorption solution. The initial and residual Li^+ concentrations in the aqueous solution were measured by atomic absorption spectrometry (AAS). The Li^+ adsorption capacity (Q, mg g^{-1}) was calculated according to eqn (1).

$$Q\,(\mathrm{mg\,g^{-1}}) = \frac{(C_0 - C_t) \times V}{m} \quad (1)$$

where C_0 (mg L^{-1}) and C_t (mg L^{-1}) are the Li^+ concentrations in the aqueous phase at the initial time and time t, respectively; V (L) is the solution volume; and m (g) is the mass of adsorbents. The adsorption rate was determined based on Q at specific time intervals. All measurements were conducted in triplicate, and the average values were taken.

2.4.2 Separation factor. In practical applications, the separation performance of adsorbents toward competing ions is crucial. The separation factor (α) is a key parameter that quantitatively describes the selective difference of the adsorbent between the target ion (Li^+) and coexisting competing ions (M^+). The calculation formula for α was calculated according to eqn (2).

$$\alpha = \frac{K_{\mathrm{d,Li^+}}}{K_{\mathrm{d,M^+}}};\ K_{\mathrm{d,Li^+}} = \frac{Q_{\mathrm{e,Li^+}}}{c_{\mathrm{e,Li^+}}};\ K_{\mathrm{d,M^+}} = \frac{Q_{\mathrm{e,M^+}}}{c_{\mathrm{e,M^+}}} \quad (2)$$

where K_d (L g^{-1}) is the distribution coefficient of ions between solid and liquid phases; Q_e (mg g^{-1}) is the Q at equilibrium time; and C_e (mg L^{-1}) is the residual ion concentration in solution after reaching adsorption equilibrium.

2.4.3 Reusability. To avoid introducing interfering ions that could affect the test results, hydrochloric acid (HCl) with the same anion (Cl^-) was selected as the eluent in the regeneration experiment. The adsorbent, after reaching saturated adsorption, was separated and then completely immersed in 0.1 mol L^{-1} HCl for desorption over 12 h, with the HCl being replaced every 6 h. After the desorption was completed, it was washed 3 times with deionized water, and then regenerated by activation at 60 °C, repeating the adsorption–desorption cycle.

2.4.4 Adsorption kinetics model. Adsorption kinetics analysis was based on the adsorption rate results. For the pseudo-first-order adsorption process, the adsorption equation can be expressed as eqn (3):[14,15]

$$\frac{\mathrm{d}Q}{\mathrm{d}t} = K_1(Q_e - Q_t) \quad (3)$$

where Q_t (mg g^{-1}) is Q at time t and K_1 (1 min^{-1}) is the pseudo-first-order adsorption rate constant.

For the pseudo-second-order adsorption process, the adsorption equation can be expressed as eqn (4):[16]

$$\frac{\mathrm{d}Q}{\mathrm{d}t} = K_2(Q_e - Q_t)^2 \quad (4)$$

where K_2 (g mg^{-1} min^{-1}) is the pseudo-second-order adsorption rate constant and C is the rate constant.

The intraparticle diffusion model is a type of kinetic model used to describe the diffusion process of substances within particles. The adsorption equation is represented as eqn (5):[17]

$$Q_t = K_i t^{1/2} + K \quad (5)$$

where K_i (mg g^{-1} $min^{-0.5}$) is the intraparticle diffusion coefficient and K (mg g^{-1}) is the intercept of the curve.

2.4.5 Adsorption isotherm model. The Langmuir adsorption isotherm model assumes monolayer adsorption on the adsorbent surface with homogeneous properties, where adsorbed molecules occupy limited sites on the surface and each site can accommodate only one molecule. The Langmuir monolayer adsorption equation is expressed as eqn (6):[18]

$$Q_e = \frac{K_L Q_{\max} c_e}{1 + K_L c_e} \quad (6)$$

where Q_{max} (mg g^{-1}) is the maximum Q in the monolayer and K_L (L mg^{-1}) is the Langmuir equilibrium constant related to free energy.

The Freundlich adsorption isotherm model assumes multilayer adsorption on the adsorbent surface with heterogeneous properties, where the affinity between the adsorbent and the adsorbate is influenced by adsorption sites. The Freundlich multilayer adsorption equation is expressed as eqn (7):[19]

$$\log Q_e = \log K_F + \frac{1}{n}\log c_e \quad (7)$$

where K_F ($L^{1/n}$ g^{-1} $mg^{-1/n-1}$) is the Freundlich equilibrium constant and n is the isotherm curvature constant.

The relevant adsorption thermodynamic parameters were calculated using the van't Hoff equation, including the Gibbs free energy change (ΔG, J mol^{-1}), enthalpy change (ΔH, J mol^{-1}), and entropy change (ΔS, J mol^{-1} K^{-1}), which qualitatively describe the reaction spontaneity, energy changes, and system disorder during the adsorption process, respectively. The calculation equations for ΔG, ΔH, and ΔS are presented as eqn (8) and (9).[8,20]

$$\Delta G^\theta = -RT \ln K_c \quad (8)$$

$$\ln K_c = \frac{\Delta S^\theta}{R} - \frac{\Delta H^\theta}{RT} \quad (9)$$

where K_c is the adsorption thermodynamic equilibrium constant. The experimental results were fitted according to the Langmuir equation, where the Langmuir equilibrium constant K_L (L mg^{-1}) was calculated based on K_c. The calculation equation is presented as eqn (10):

$$K_c = M_\omega \times 55.5 \times K_L \quad (10)$$

where M_ω (g mol^{-1}) is the molecular weight of the adsorbate.

3. Results and discussion

3.1 Characterization of Li/NH_2/MIL-101(Cr) and Li/NH_2/MIL-100(Fe)

Characterization of MIL-101(Cr), MIL-100(Fe), and their derivatives was performed using XRD, FT-IR, XPS, SEM, BET, and TG. Fig. 3(a and b) presents the XRD patterns, and Fig. 3(c and d) shows the FT-IR spectra. The central characteristic peaks of MIL-101(Cr) are at 2θ = 5.8°, 8.4°, and 9.4°, and those of MIL-100(Fe) are at 2θ = 10.2°, 11.0°, 14.2°, 20.1°, and 24.1°. It is worth noting that in the XRD patterns of MIL-101(Cr) and its derivatives, a characteristic peak of H_2BDC appears at 17.5°, indicating that residual H_2BDC was not completely removed during the post-treatment process. The characteristic peak at around 27° reflects the arrangement law of secondary structural units in the crystal. The results demonstrate that neither the optimized mineralizer synthesis system nor the introduction of amino-functionalized ligands significantly altered the crystal structure of adsorbents. However, upon –NH_2 functionalization, partial pore filling within the framework led to moderately reduced crystallinity, as evidenced by noticeable peak broadening in the characteristic diffraction patterns. Additionally, the decreased intensity of certain characteristic peaks suggests slight structural degradation of the crystal framework.[21,22] After amination modification, the FT-IR spectrum of the material shows several new absorption peaks: the absorption peak cluster in the range of 3500–3300 cm^{-1} is attributed to the symmetric and asymmetric stretching vibrations of –NH_2, and the absorption peak at around 1250 cm^{-1} corresponds to the C–N stretching vibration in the molecular structure.

Fig. 4(a and b) displays the full-scan XPS spectra and high-resolution spectra of C 1s, O 1s, Cr 2p/Fe 2p, and Li 1s for MIL-101(Cr) and its derivatives, respectively. The characterization results reveal distinct N 1s signals, confirming the successful amination modification. In the Li 1s high-resolution spectrum, a distinct characteristic peak appears at around 56 eV, confirming the participation of $LiNO_3$ in the synthesis reaction. No lithium signals are observed in the full-scan XPS spectrum, possibly due to their low concentration. Fig. 4(c and d) display the full-scan XPS spectra and high-resolution spectra of C 1s, O 1s, Fe 2p, and Li 1s of MIL-100(Fe) and its derivatives, respectively, with results analogous to those of MIL-101(Cr).

The SEM characterization results of MIL-101(Cr), MIL-100 (Fe), and their derivatives are shown in Fig. 5(a and b). Both

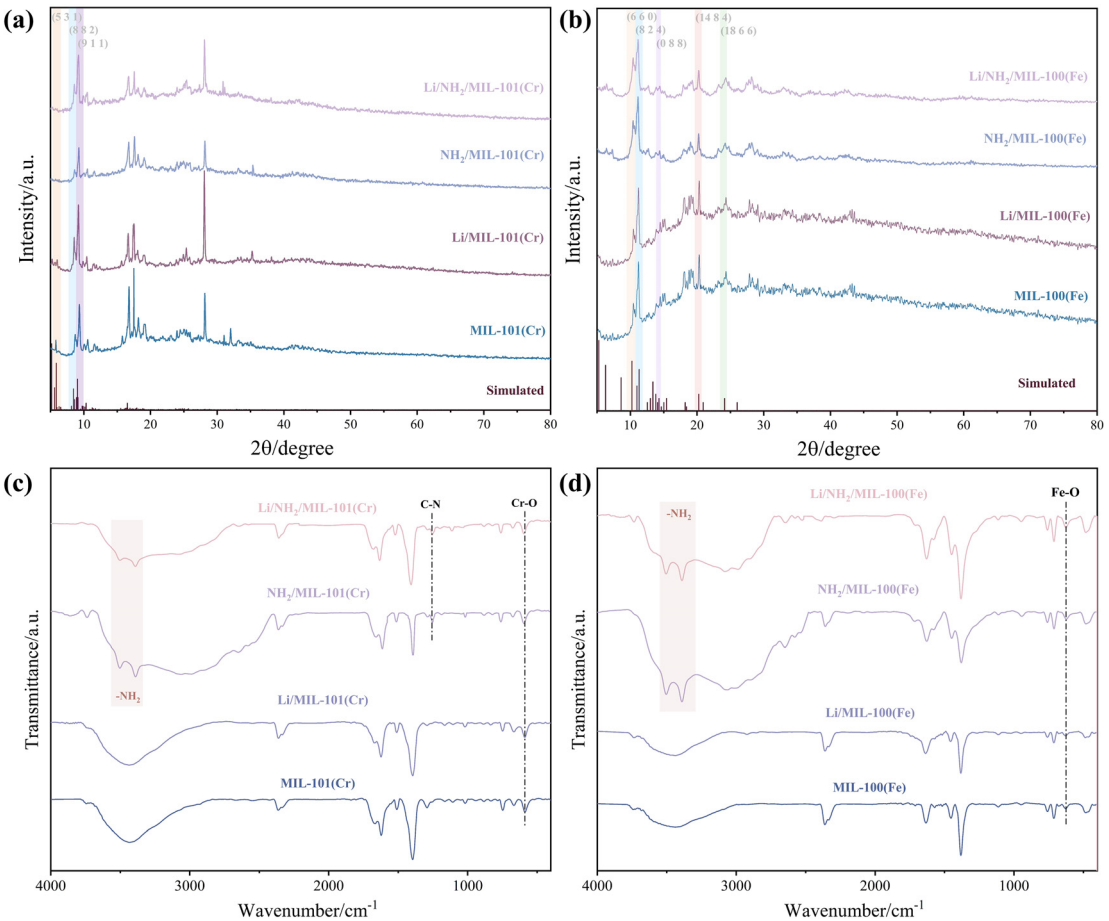

Fig. 3 XRD pattern (a), (b) and FT-IR spectra (c), (d) of the MIL-101(Cr), MIL-100(Fe), and their derivatives.

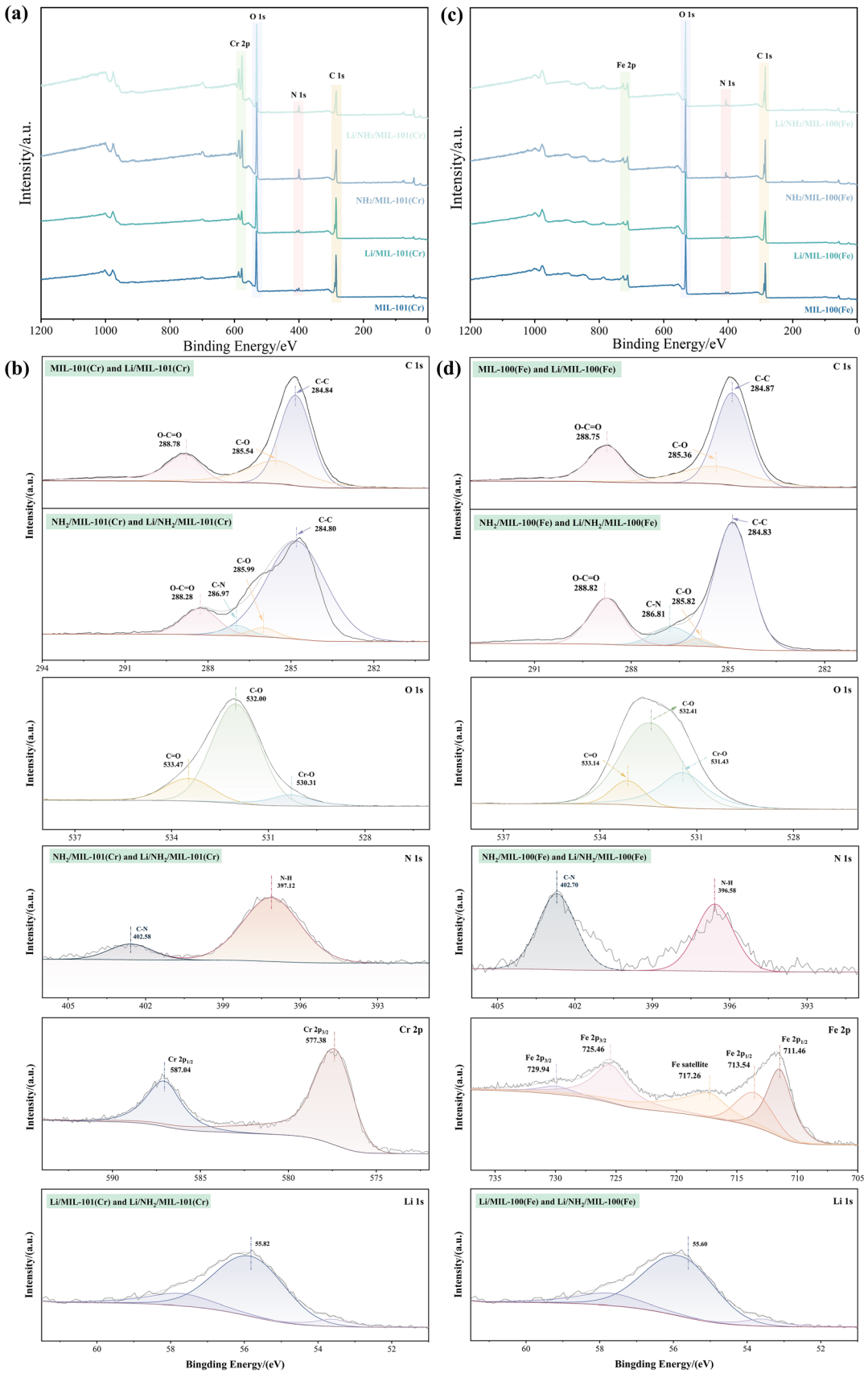

Fig. 4 XPS survey spectra (a) and (c), and C 1s, O 1s, N 1s, Cr 2p/Fe 2p and Li 1s scan spectra (b) and (d) of MIL-101(Cr), MIL-100(Fe), and their derivatives.

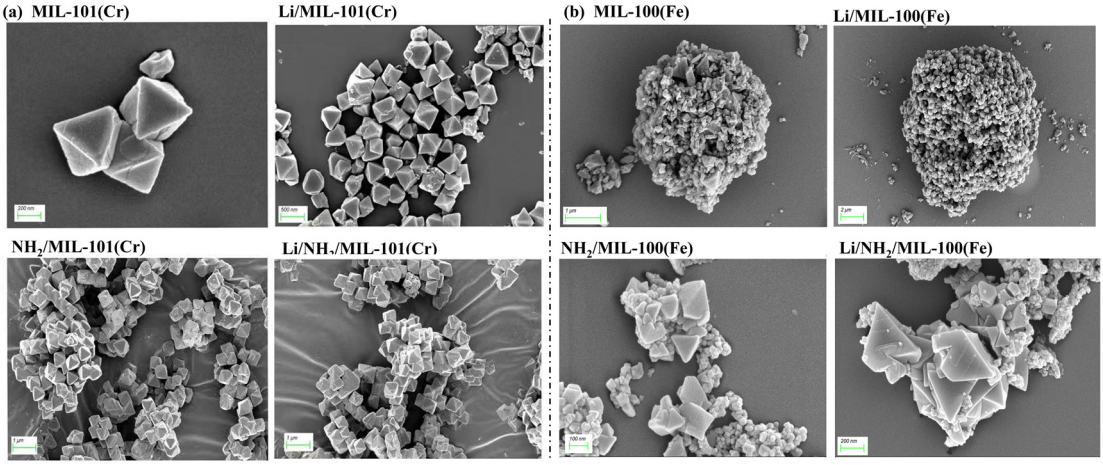

Fig. 5 SEM of MIL-101(Cr) (a), MIL-100(Fe) (b), and their derivatives.

MIL-101(Cr) and Li/MIL-101(Cr) exhibit typical octahedral crystal grains,[23] indicating that $LiNO_3$ as a mineralizer does not alter the crystal morphology within certain concentration ranges. Compared to MIL-101(Cr), the particle size of Li/MIL-101(Cr) is reduced, which can be attributed to the decreased average crystal dimensions caused by increased mineralizer concentration.[24] After $-NH_2$ introduction, obvious particle aggregation occurs. MIL-100(Fe) particles show poor morphological regularity and severe aggregation. After introducing $LiNO_3$ as a mineralizer, the morphological regularity of Li/MIL-100(Fe) significantly improves, comprising aggregated small particles with well-defined octahedral crystal structures. Following $-NH_2$ functionalization, partial destruction of the octahedral structure is observed, consistent with the XRD results. The crystal sizes become non-uniform, with notably enlarged grains and weakened aggregation phenomena.

The pore characteristic parameters of MIL-101(Cr), MIL-100(Fe), and their derivatives are listed in Table 1, with their corresponding adsorption–desorption isotherms and pore size distributions shown in Fig. 6(a and b). The N_2 adsorption–desorption isotherms of both MIL-101(Cr) and Li/MIL-101(Cr) exhibit Type I characteristics with minor hysteresis loops, likely resulting from partial mesopore formation caused by crystal stacking.[25] This confirms that the adsorbents are mesoporous materials with narrow pore size distributions. Similarly, NH_2/MIL-101(Cr) and Li/NH_2/MIL-101(Cr) display Type I isotherms featuring nearly horizontal parallel H4-type hysteresis loops, indicative of their microporous nature.[26,27] For MIL-100(Fe) and its derivatives, all N_2 adsorption–desorption isotherms also follow Type I behavior. Amino-functionalization induces decreases in S_{BET}, the BJH pore volume, and pore size, which may be attributed to structural distortions in NH_2/MIL-100(Fe) caused by the inherent structural disparity between H_3BTC and 2-NH_2-BDC. In particular, the S_{BET} of Li/NH_2/MIL-100(Fe) exhibits a significant increase, which is attributed to the synergistic mineralization and templating effects.

Table 1 Pore characteristic parameters of MIL-101(Cr), MIL-100(Fe), and their derivatives

Parameters	S_{BET} ($m^2\ g^{-1}$)	BJH pore volume ($cm^3\ g^{-1}$)	Pore size (nm)
MIL-101(Cr)	2252.314	1.262	2.001
Li/MIL-101(Cr)	2392.657	1.397	1.901
NH_2/MIL-101(Cr)	2567.879	1.561	5.865
Li/NH_2/MIL-101(Cr)	2681.138	1.833	3.858
MIL-100(Fe)	1489.381	0.816	2.192
Li/MIL-100(Fe)	1625.369	0.958	2.358
NH_2/MIL-100(Fe)	1408.340	0.708	2.012
Li/NH_2/MIL-100(Fe)	2454.680	1.304	2.125

The TG results of MIL-101(Cr), MIL-100(Fe), and their derivatives are shown in Fig. 7(a–d). The mass loss primarily occurs in several stages: (1) evaporation of free water molecules within the adsorbent; (2) decomposition of residual H_2BDC within the adsorbent;[28] (3) degradation of organic ligands of the adsorbent;[29] and (4) complete collapse of the metal–ligand framework structure, followed by carbonization at elevated temperatures. Collectively, these results indicate that the introduction of $-NH_2$ groups and $LiNO_3$ as a mineralizer enhances the thermal stability of the adsorbent.

3.2 Li^+ adsorption performance

3.2.1 Effect of $LiNO_3$ dosage on the adsorption capacity. Under identical experimental conditions – initial Li^+ concentration of 10 g L^{-1}, adsorbent concentration of 2 g L^{-1}, adsorption temperature of 298.15 K, adsorption time of 8 h, and unadjusted pH value – the Li^+ adsorption capacities of MIL-101(Cr), MIL-100(Fe), and their derivatives are presented in Fig. 8(a and b).

Both Li/MIL-101(Cr) and Li/NH_2/MIL-101(Cr) exhibit maximum Li^+ adsorption capacities at $w(LiNO_3)$ = 0.75 wt%, reaching 36.69 and 41.25 mg g^{-1}, respectively. For Li/MIL-101(Cr), the adsorption capacity first increases and then decreases with increasing $LiNO_3$ dosage. As the $LiNO_3$ concentration

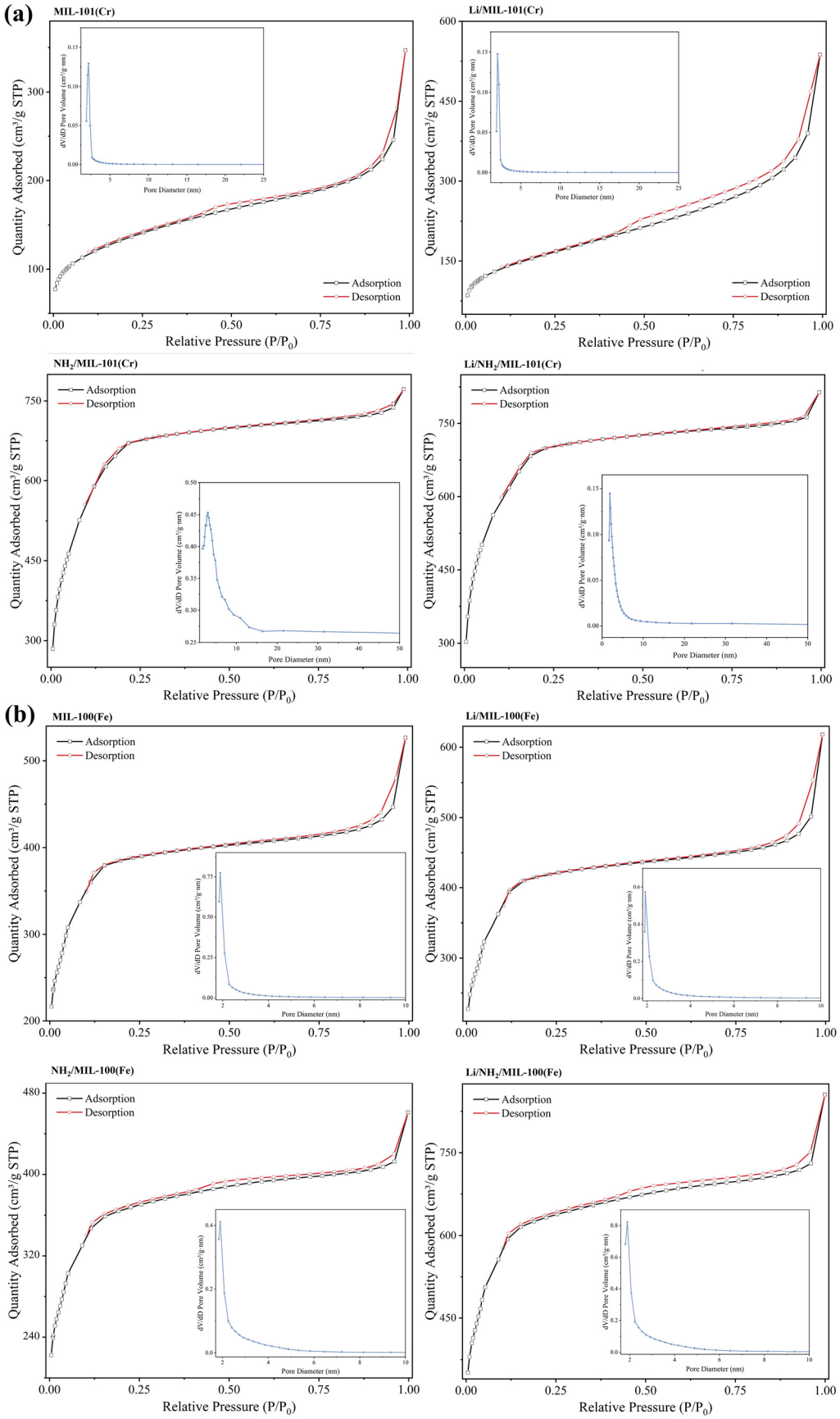

Fig. 6 N_2 adsorption–desorption isotherm and pore diameter distribution diagram of MIL-101(Cr) (a), MIL-100(Fe) (b), and their derivatives.

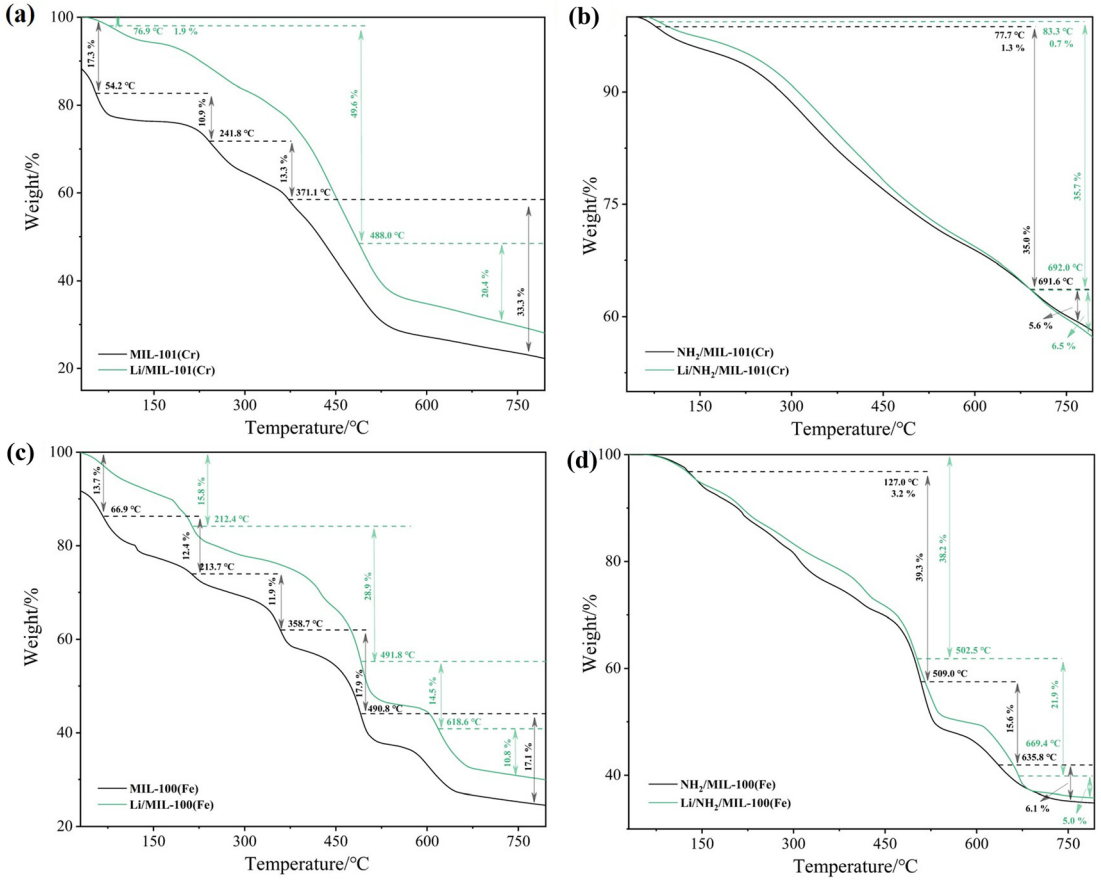

Fig. 7 TGA curve of the MIL-101(Cr) (a and b), MIL-100(Fe) (c and d), and their derivatives.

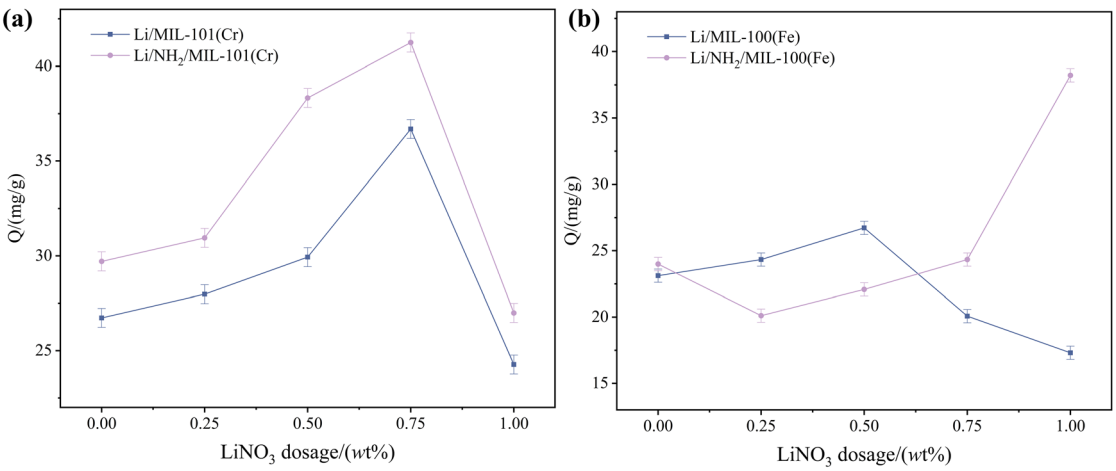

Fig. 8 Li^+ adsorption capacities of MIL-101(Cr) (a), MIL-100(Fe) (b), and their derivatives at different $LiNO_3$ dosages.

increases, the mineralization effect becomes apparent, promoting the formation of smaller and more regular crystals. However, excessive $LiNO_3$ induces structural defects and pore blockage, and may produce byproducts that hinder Li^+ accessibility, leading to reduced adsorption capacity. Furthermore, NH_2/MIL-101(Cr) exhibits enhanced adsorption capacity after amination, primarily due to two mechanisms: (1) $-NH_2$ being an electron-donating group where the N atom possesses lone pair electrons that can act as Lewis bases to form coordination bonds with Li^+;[30–32] and (2) amination enlarges S_{BET} (providing more adsorption sites) and pore size (effectively reducing Li^+ mass transfer resistance within the framework channels).

For Li/MIL-100(Fe), the maximum Li^+ adsorption capacity is achieved at $w(LiNO_3)$ = 0.5 wt%, while Li/NH_2/MIL-100(Fe) reaches its peak capacity at $w(LiNO_3)$ = 1.0 wt%, with values of 26.73 and 38.22 mg g^{-1}, respectively. The Li^+ adsorption trend of Li/MIL-100(Fe) resembles that of Li/MIL-101(Cr). Notably, for NH_2/MIL-100(Fe), the Li^+ adsorption capacity first decreases and then increases with increasing $LiNO_3$ dosage. The reason is as follows: the introduced lithium source forms weak coordination bonds with $-NH_2$ or uncoordinated $-COO^-$ moieties, which hinders the amination process and reduces the availability of active Li^+ adsorption sites.[32–34] The enhanced mineralization effect at higher $LiNO_3$ concentrations promotes the formation of more ordered framework structures, thereby improving the adsorption performance. However, as the dosage of $LiNO_3$ increases, the mineralization effect becomes more obvious. At higher $LiNO_3$ concentrations, the enhanced mineralization effect promotes the formation of more ordered framework structures, thereby improving the adsorption performance.

Evidently, amination and the introduction of an appropriate $LiNO_3$ dosage effectively enhance the Li^+ adsorption capacity of the adsorbents. The difference in Li^+ adsorption capacities between Li/NH_2/MIL-101(Cr) and Li/NH_2/MIL-100(Fe) stems from variations in the coordination strength of the metal sites (Cr^{3+} *vs.* Fe^{3+}), degree of amination, and steric hindrance differences of the organic ligands.

3.2.2 Effect of the initial Li^+ concentration and temperature on the adsorption capacity. The Li^+ adsorption capacities of Li-0.75/NH_2/MIL-101(Cr) and Li-1.0/NH_2/MIL-100(Fe) at environmental temperatures of 293.15 K, 298.15 K, 303.15 K, and 308.15 K for solutions with different initial Li^+ concentrations (0.5, 1, 2, 5, and 10 g L^{-1}) are shown in Fig. 9(a and b). Under identical temperatures, the Li^+ adsorption capacity increases with rising initial Li^+ concentrations. When the initial concentration reaches 10 g L^{-1}, the adsorption capacity of Li-0.75/NH_2/MIL-101(Cr) approaches a plateau, while that of Li-1.0/NH_2/MIL-100(Fe) continues to exhibit an upward trend. This indicates that Li-1.0/NH_2/MIL-100(Fe) requires higher Li^+ initial concentrations to achieve saturation, whereas Li-0.75/NH_2/MIL-101(Cr) is more suitable for adsorption in low Li^+ concentration solutions. At constant initial Li^+ concentrations, the adsorption capacity decreases with increasing temperature, confirming the exothermic nature of Li^+ adsorption by these adsorbents. As the temperature of the aqueous solution rises, the intensified molecular thermal motion weakens the interactions between the adsorbent surfaces and adsorbate molecules.[8,35]

3.2.3 Effect of adsorbent dosage on the adsorption capacity. Fig. 10 illustrates the Li^+ adsorption capacities at varying Li-0.75/NH_2/MIL-101(Cr) and Li-1.0/NH_2/MIL-100(Fe) concentrations (0.5, 1, 2, and 5 g L^{-1}). With increasing adsorbent dosage, the number of available adsorption sites increases, leading to a significant enhancement in Li^+ adsorption capacity. As the dosage continues to increase, the collision probability between Li^+ ions and surface functional groups intensifies, while the concentration gradient-driven migration force strengthens, causing the growth rate of the adsorption capacity to slow and eventually stabilize. However, excessive adsorbent dosage leads to a slight decrease in the adsorption capacity due to hindered diffusion of adsorbate molecules and increased steric hindrance effects.

3.2.4 Effect of pH of solvent on the adsorption capacity. Under adsorption conditions, solution pH values were set at 3, 5, 7, 9, and 11, along with the unadjusted pH values: $pH_{Li\text{-}0.75/NH2/MIL\text{-}101(Cr)}$ = 6.86 and $pH_{Li\text{-}1.0/NH2/MIL\text{-}100(Fe)}$ = 5.71. As depicted in Fig. 11(a and b), upon increasing the pH, both adsorbents demonstrate a trend of initial increase followed by a decrease in the Li^+ adsorption capacity. Li-0.75/NH_2/MIL-101(Cr) achieves its maximum Li^+ adsorption capacity of 43.58 mg g^{-1} at pH 7, while Li-1.0/NH_2/MIL-100(Fe) reaches its peak Li^+ adsorption capacity of 38.22 mg g^{-1} at the unadjusted pH 5.71.

Under acidic conditions, partial M–OH or $-NH_2$ groups in the frameworks of Li-0.75/NH_2/MIL-101(Cr) and Li-1.0/NH_2/

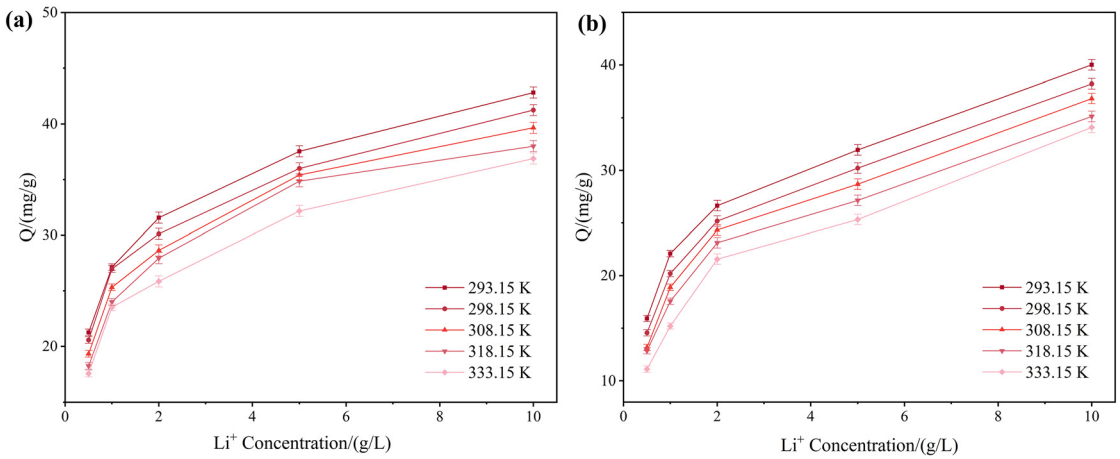

Fig. 9 Li^+ adsorption capacities of Li-0.75/NH_2/MIL-101(Cr) (a) and Li-1.0/NH_2/MIL-100(Fe) (b) at different temperatures and initial Li^+ concentrations.

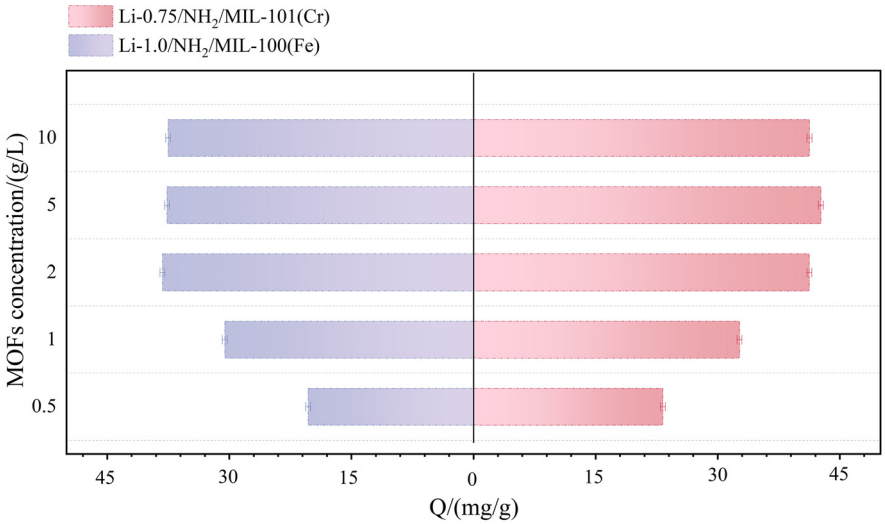

Fig. 10 Li^+ adsorption capacities of Li-0.75/NH_2/MIL-101(Cr) and Li-1.0/NH_2/MIL-100(Fe) at different adsorbent dosages.

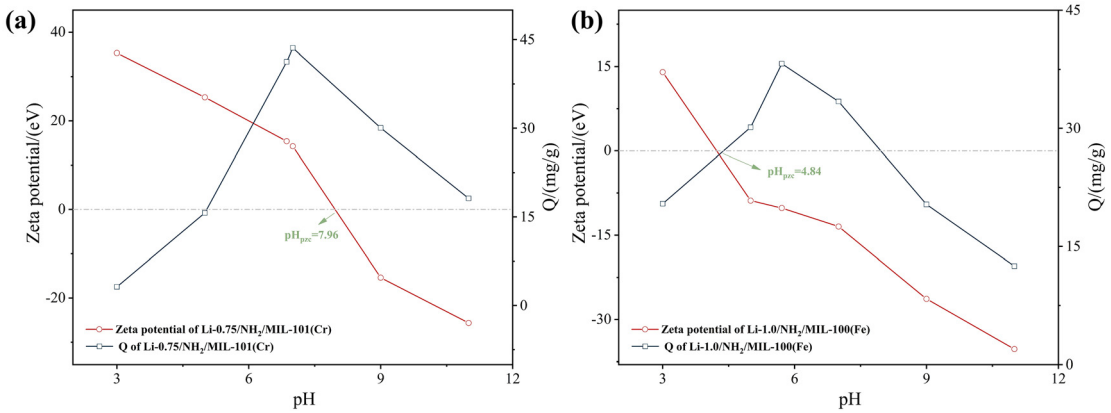

Fig. 11 Q_{Li} and zeta potential of Li-0.75/NH_2/MIL-101(Cr) (a) and Li-1.0/NH_2/MIL-100(Fe) (b) at different solution pH values.

MIL-100(Fe) undergo protonation, forming M–OH_2^+ or –NH_3^+. Stronger acidity enhances the protonation degree, leading to more positive surface charges that electrostatically repel Li^+ ions.[36] As the pH increases, protonation diminishes until the pH exceeds the pH of zero point charge (pH_{pzc}), where –COOH, –NH_2, or minor M–OH groups deprotonate to form –COO^-, –NH^-, or M–O^-. These deprotonated groups exhibit dipole moments and enable Li^+ adsorption through ion–dipole interactions. However, under excessively alkaline conditions, the adsorption capacity declines alongside unstable zeta potential values, likely attributable to framework degradation (*e.g.*, hydrolysis or formation of metal hydroxides for M–O bonds[37]). The pH_{pzc} follows the order: Li-0.75/NH_2/MIL-101(Cr) > 7 > Li-1.0/NH_2/MIL-100(Fe). Notably, Li-0.75/NH_2/MIL-101(Cr) displays a more pronounced adsorption decline under acidic conditions, while Li-1.0/NH_2/MIL-100(Fe) experiences more severe adsorption reduction under alkaline conditions. This suggests that Li-0.75/NH_2/MIL-101(Cr) can still undergo protonation at relatively higher pH values, whereas Li-1.0/NH_2/MIL-100(Fe) maintains deprotonation capability at lower pH levels.

In conclusion, the solution pH does influence the adsorption performance of the adsorbents. The optimal pH range for Li-0.75/NH_2/MIL-101(Cr) is 7–9, while that for Li-1.0/NH_2/MIL-100(Fe) is 5–7.

3.2.5 Adsorption kinetics. The adsorption rates are shown in Fig. 12(a). At each stage, Li-0.75/NH_2/MIL-101(Cr) demonstrates higher adsorption capacity and faster adsorption kinetics, reaching equilibrium in approximately 90 minutes. Kinetic models (pseudo-first-order, pseudo-second-order, and intraparticle diffusion) for both materials are shown in Fig. 12 (b–d). Moreover, the corresponding model parameters are systematically summarized in Tables 2–4, enabling a detailed quantitative analysis of the adsorption processes.

Notably, the pseudo-second-order kinetic model exhibits higher correlation coefficients (R^2) for Li-0.75/NH_2/MIL-101 (Cr), with its theoretical Li^+ adsorption capacity ($Q_{e,th}$) closely aligning with the experimental values ($Q_{e,ex}$). This indicates

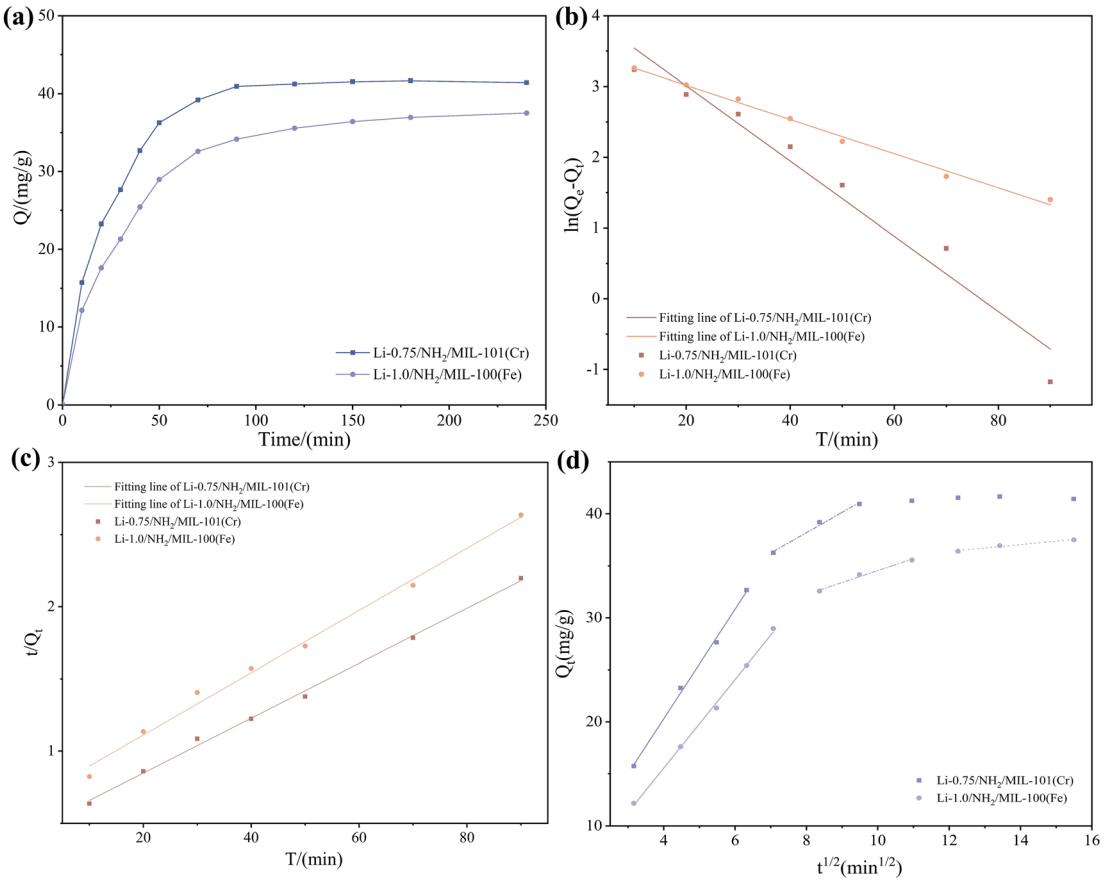

Fig. 12 The adsorption rate (a), pseudo-first-order kinetic model (b), pseudo-second-order kinetic model (c) and intraparticle diffusion model (d) of Li-0.75/NH_2/MIL-101(Cr) and Li-1.0/NH_2/MIL-100(Fe).

Table 2 The parameters of the pseudo-first-order kinetic model of Li-0.75/NH_2/MIL-101(Cr) and Li-1.0/NH_2/MIL-100(Fe)

	The pseudo-first-order kinetic model			
Parameters	$Q_{e,ex}$ (mg g^{-1})	$K_1 \times 10$ (1 min^{-1})	$Q_{e,th}$ (mg g^{-1})	R^2
Li-0.75/NH_2/MIL-101(Cr)	41.25	0.532	58.84	0.95
Li-1.0/NH_2/MIL-100(Fe)	38.22	0.242	33.17	0.99

Table 3 The parameters of pseudo-second-order kinetic model of Li-0.75/NH_2/MIL-101(Cr) and Li-1.0/NH_2/MIL-100(Fe)

	The pseudo-second-order kinetic model			
Parameters	$Q_{e,ex}$ (mg g^{-1})	$K_2 \times 10^3$ (g mg^{-1} min^{-1})	$Q_{e,th}$ (mg g^{-1})	R^2
Li-0.75/NH_2/MIL-101(Cr)	41.25	0.777	52.52	0.99
Li-1.0/NH_2/MIL-100(Fe)	38.22	0.684	46.36	0.99

Table 4 The parameters of the intraparticle diffusion model of Li-0.75/NH_2/MIL-101(Cr) and Li-1.0/NH_2/MIL-100(Fe)

Materials	Parameters		
Li-0.75/NH_2/MIL-101(Cr)	$K_{i,1}$	K_1	R^2
	5.269	−0.776	0.99
	$K_{i,2}$	K_2	R^2
	1.942	22.673	0.99
Li-1.0/NH_2/MIL-100(Fe)	$K_{i,1}$	K_1	R^2
	4.267	−1.524	0.99
	$K_{i,2}$	K_2	R^2
	1.146	23.103	0.99
	$K_{i,3}$	K_3	R^2
	0.331	32.426	0.98

that the pseudo-second-order model provides a superior description of the Li^+ adsorption process for Li-0.75/NH_2/MIL-101(Cr),[38] suggesting that chemisorption is the dominant mechanism throughout the adsorption process. Specifically, Li-0.75/NH_2/MIL-101(Cr) possesses larger window and pore sizes, while chemisorption dominates the entire adsorption process. This is because it has a stronger amination degree, with $-NH_2$ groups playing a dominant role in chemisorption during the initial stage. For Li-1.0/NH_2/MIL-100(Fe), both pseudo-first-order and pseudo-second-order kinetic models are applicable, implying synergistic interactions between initial physisorption and mid-to-late stage chemisorption during the adsorption process.[39,40]

The intraparticle diffusion model analysis shows that $K \neq 0$, indicating that internal diffusion is not the sole rate-limiting step and that the adsorption mass transfer is governed by multiple rate-controlling factors.[41] For both adsorbents, the negative first-stage K values highlight the inapplicability of the intraparticle diffusion model during this phase. This can be attributed to Li^+ diffusing from the aqueous phase to the adsorbent surface driven by concentration gradients, where it is rapidly captured by surface active sites. In this stage, surface adsorption occurs much faster than intraparticle diffusion, leading to a significant increase in Q_e at smaller $t^{1/2}$ values.[42] As Li^+ migrates into the adsorbent interior, the adsorption process enters an intraparticle diffusion-dominated stage, during which adsorbates diffuse through mesopores. With $K_{i,2} > K_{i,3}$ and $K_3 > K_2$, the occupation of surface adsorption sites by Li^+ enhances mass transfer resistance, thereby slowing the adsorption rate. Finally, as Li^+ continues to migrate through micropores and the available active sites within the adsorbent become saturated, the system approaches adsorption equilibrium.

3.2.6 Adsorption thermodynamics. The Langmuir and Freundlich adsorption isotherm models are shown in Fig. 13(a and b), with the corresponding parameters being tabulated in Tables 5 and 6, respectively.

Table 5 The parameters of the Langmuir adsorption isotherm model of Li-0.75/NH_2/MIL-101(Cr) and Li-1.0/NH_2/MIL-100(Fe)

Parameters	T (K)	Q_{max} (mg g^{-1})	K_L (L mg^{-1})	R^2
Li-0.5/UIO-66	293.15	45.39	1.350	0.99
	298.15	43.61	1.347	0.99
	308.15	42.21	1.330	0.99
	318.15	40.58	1.312	0.99
	333.15	39.31	1.222	0.99
Li-0.75/HKUST-1	293.15	43.28	0.883	0.99
	298.15	41.62	0.823	0.99
	308.15	40.31	0.775	0.98
	318.15	38.44	0.765	0.98
	333.15	38.02	0.633	0.98

The Langmuir adsorption isotherm model provides a better description of the adsorption behavior for both adsorbents, likely due to the uniform distribution of active adsorption sites on their surfaces, which confirms the monolayer adsorption of Li^+ during the process. Combined with the results of adsorption kinetic models, it can be concluded that Li-0.75/NH_2/MIL-101(Cr) exhibits monolayer chemisorption of Li^+, whereas Li-1.0/NH_2/MIL-100(Fe) demonstrates a combination of monolayer chemisorption and physisorption. Additionally,

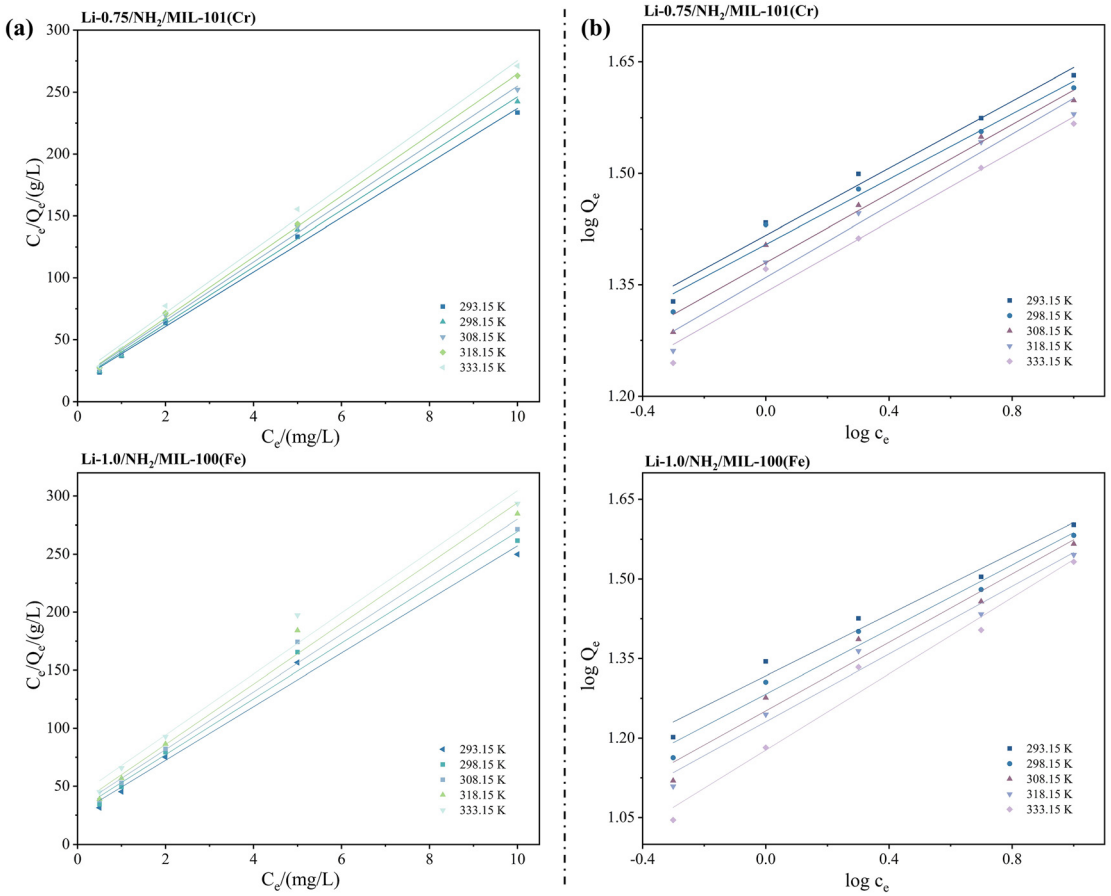

Fig. 13 Linear fitting of the Langmuir adsorption isotherm model (a) and the Freundlich adsorption isotherm model (b) of Li-0.75/NH_2/MIL-101(Cr) and Li-1.0/NH_2/MIL-100(Fe).

Table 6 The parameters of the Freundlich adsorption isotherm model of Li-0.75/NH_2/MIL-101(Cr) and Li-1.0/NH_2/MIL-100(Fe)

Parameters	T (K)	n	K_F ($L^{1/n}$ g^{-1} $mg^{-1/n-1}$)	R^2
Li-0.5/UIO-66	293.15	4.426	26.096	0.98
	298.15	4.547	25.366	0.97
	308.15	4.302	23.981	0.97
	318.15	4.143	22.906	0.96
	333.15	4.241	21.901	0.96
Li-0.75/HKUST-1	293.15	3.460	20.771	0.97
	298.15	3.281	19.182	0.97
	308.15	3.098	17.842	0.93
	318.15	3.131	17.016	0.97
	333.15	2.782	15.044	0.94

in the Freundlich adsorption isotherm model, $n > 1$ indicates a nonlinear isotherm, suggesting heterogeneous adsorption where attractive forces between the adsorbate and functional groups on the adsorbent surface facilitate the adsorption process.[43,44] The decrease in K_F with increasing temperature confirms the exothermic nature of the adsorption, reflecting reduced affinity between the adsorbent and the adsorbate.

Furthermore, thermodynamic parameters including Gibbs free energy change (ΔG), enthalpy change (ΔH), and entropy change (ΔS) were calculated to investigate the Li^+ adsorption process. Fig. 14 shows the linear fitting results of the van't Hoff equation for Li-0.75/NH_2/MIL-101(Cr) and Li-1.0/NH_2/MIL-100(Fe), with the corresponding thermodynamic parameters being summarized in Table 7. $\Delta G < 0$ indicates that the adsorption process is spontaneous. $\Delta H < 0$ demonstrates that Li^+ adsorption by the adsorbent is exothermic. $\Delta S > 0$ confirms increased randomness during adsorption, with Li^+ undergoing random adsorption on the adsorbent surface.

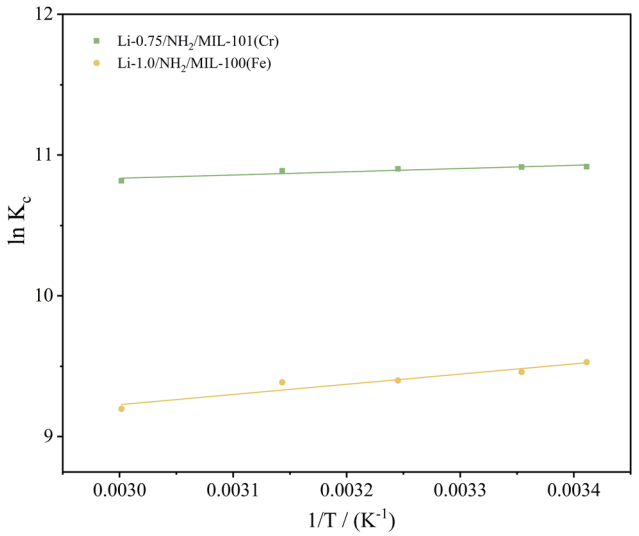

Fig. 14 Linear fitting of the van't Hoff equation of Li-0.75/NH_2/MIL-101 (Cr) and Li-1.0/NH_2/MIL-100(Fe).

3.2.7 Reusability. To assess the cyclic stability of the adsorbents, four regeneration cycles were performed for Li-0.75/NH_2/MIL-101(Cr) and Li-1.0/NH_2/MIL-100(Fe), as illustrated in Fig. 15(a and b). After the adsorption–desorption cycles, both adsorbents exhibited decreased adsorption capacities, indicating that partial framework structures underwent irreversible collapse during the desorption–regeneration process or that incomplete desorption hindered the full recovery of adsorption sites.[45] Li-0.75/NH_2/MIL-101(Cr) demonstrated superior reusability compared to Li-1.0/NH_2/MIL-100(Fe), maintaining over 90% of its initial adsorption capacity after four cycles. The framework stability of Li-0.75/NH_2/MIL-101(Cr) is attributed to the strong coordination between Cr^{3+} and H_2BDC, while $LiNO_3$ as a mineralizer enhances crystal regularity and crystallinity. Additionally, amination contributes to the improved structural stability of the adsorbent.[46] For Li-1.0/NH_2/MIL-100(Fe), the introduction of $LiNO_3$ may enhance chemical stability by promoting crystal densification, although Fe^{3+} leaching remains possible during adsorption–desorption cycles.

3.2.8 Mechanism of Li^+ adsorption. SEM image of Li-0.75/NH_2/MIL-101(Cr) after Li^+ adsorption is presented in Fig. 16. Although the morphology showed no significant changes post-adsorption, surface cracks were observed. These cracks may originate from the stress generated during synthesis and post-processing, leading to fracturing during adsorption or desorption. Nevertheless, since adsorption does not occur exclusively on the surface, the formation of cracks does not substantially impact cycling performance; instead, it may expose additional coordination sites.

Cage-type MOFs are characterized by small aperture windows and large cavities. The size-sieving effect regulates the entry of target ions, while the spacious cavities facilitate diffusion, endowing MOFs with substantial pore volume. To visually illustrate the accessibility of Li^+ into the cavities of Li-0.75/NH_2/MIL-101(Cr), simplified structural units were constructed. The molecular structure and mesoporous cages of Li-0.75/NH_2/MIL-101(Cr) are depicted in Fig. 17. This material adopts a super-tetrahedral cubic unit cell containing two types of cages with free internal diameters of ~29 Å and 34 Å (in a 2 : 1 ratio), interconnected by windows measuring ~12–16 Å.[47] With its small hydrated radius (0.382 nm) and ionic radius

Table 7 The thermodynamic parameters of Li-0.5/UIO-66 and Li-0.75/HKUST-1

			ΔG^θ (kJ mol^{-1})				
Parameters	ΔH^θ (kJ mol^{-1})	ΔS^θ (kJ mol^{-1})	293.15 K	298.15 K	308.15 K	318.15 K	333.15 K
Li-0.5/UIO-66	−84.34	1.91	−26.61	−27.06	−27.93	−28.80	−29.96
Li-0.75/HKUST-1	−58.62	6.03	−23.23	−23.45	−24.08	−24.83	−25.48

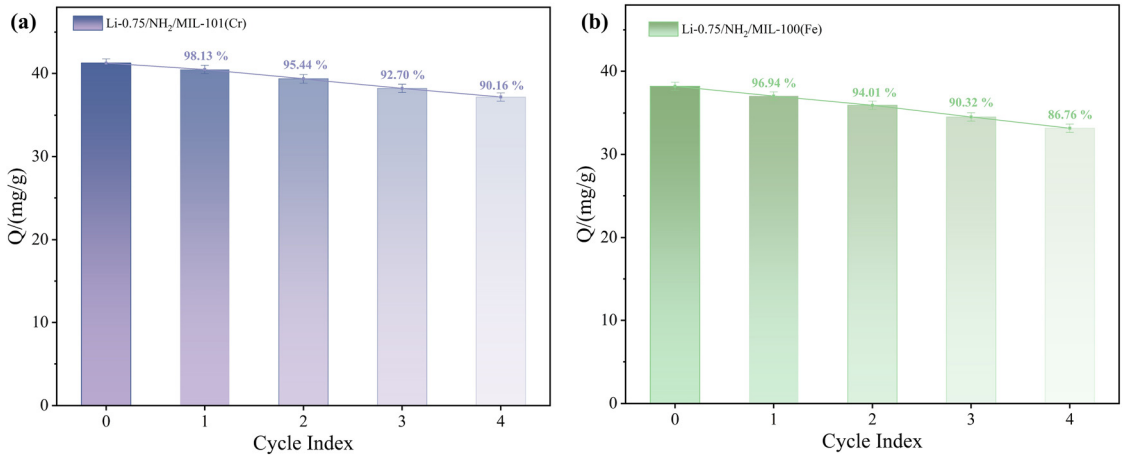

Fig. 15 The reusability of Li-0.75/NH_2/MIL-101(Cr) (a) and Li-1.0/NH_2/MIL-100(Fe) (b).

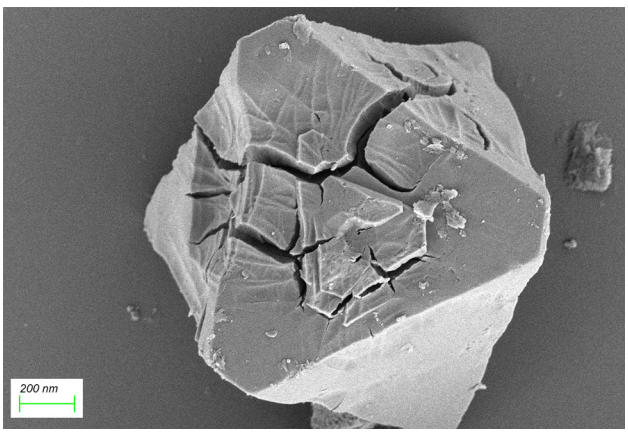

Fig. 16 SEM image of Li-0.75/NH_2/MIL-101(Cr) after adsorption.

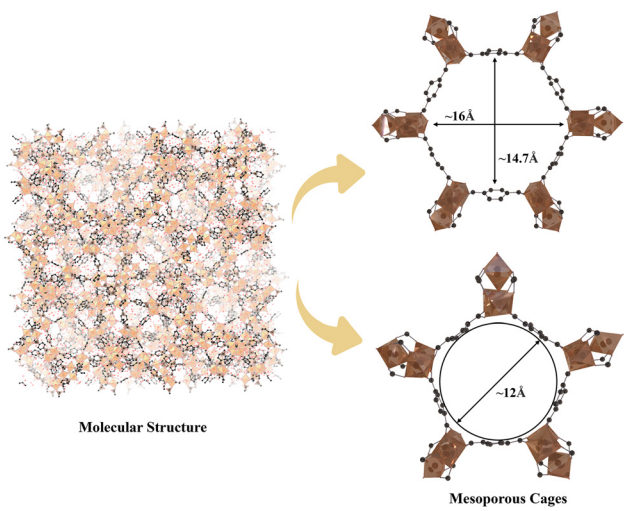

Fig. 17 Molecular structure and windows of the mesoporous cage for MIL-101(Cr).

(0.076 nm), Li^+ can freely traverse the windows into the cavities and rapidly migrate through the framework channels, establishing pore filling as one of the primary adsorption mechanisms.

Building on the aforementioned pH-dependent adsorption results, under unadjusted solution pH conditions, the adsorbent surface carries positive charges that exert repulsive forces on Li^+. Despite this, Li-0.75/NH_2/MIL-101(Cr) retains decent Li^+ adsorption capacity in such an environment, and adsorption capacity varies with pH, suggesting that although electrostatic attraction contributes to the process, it does not dominate the primary adsorption mechanism. Fig. 18(a and b) shows the FT-IR and XPS results of Li-0.75/NH_2/MIL-101(Cr) after Li^+ adsorption.

The FT-IR characteristic peaks remain basically consistent before and after adsorption. However, slight blue shifts are observed in the symmetric and asymmetric vibrational absorption peaks of $-COO^-$ in the range of 1650–1550 cm^{-1}, as well as in the $-NH_2$ and C–N characteristic peaks, indicating that the structural $-NH_2$ groups and unsaturated $-COO^-$ may participate in adsorption *via* weak coordination.[13] In the XPS spectra, the C 1s characteristic peaks exhibit no significant changes, and due to the low sensitivity of lithium to chemical environments, the Li 1s binding energy shift is negligible. For the O 1s, Cr 2p, and N 1s spectra, all characteristic peaks shift toward higher binding energies, suggesting that Cr^{3+} (or Cr–O^-), $-NH_2$, and $-COO^-$ may form weak coordination bonds with Li^+. Collectively, Li^+ adsorption by Li-0.75/NH_2/MIL-101(Cr) is a complex process driven by the synergistic effects of multiple interactions, including pore filling, electrostatic attraction, and coordination interactions. In addition, the adsorption mechanism of Li-1.0/NH_2/MIL-100(Fe) is similar to that of Li-0.75/NH_2/MIL-101(Cr).

3.2.9 Comparison of Li^+ adsorption capacities with other MOFs. Table 8 compares the Li^+ extraction capacities of Li-0.75/NH_2/MIL-101(Cr) and Li-1.0/NH_2/MIL-100(Fe) with other

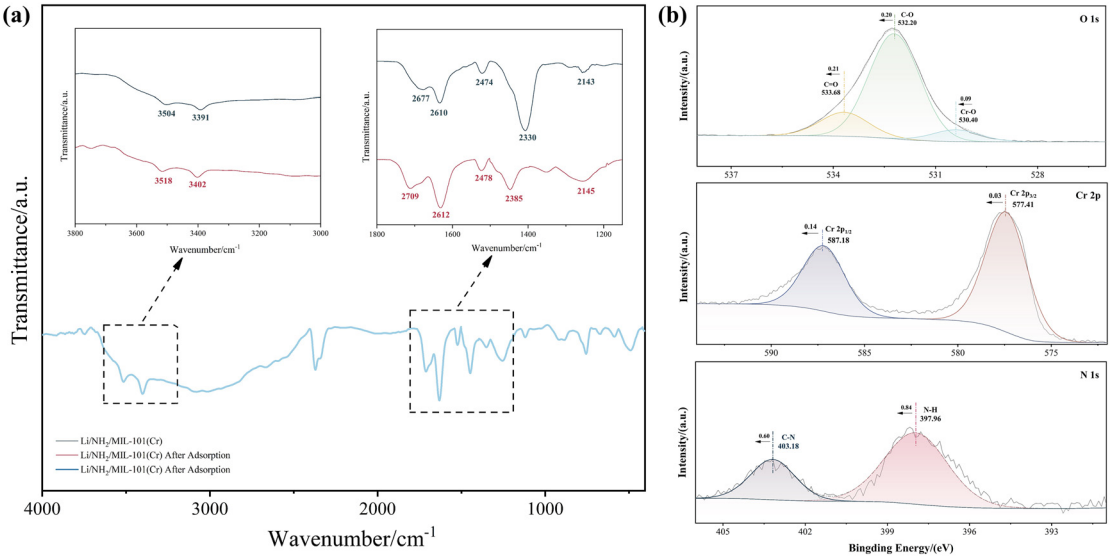

Fig. 18 FT-IR spectra (a) and O 1s, Cr 2p and N 1s scan spectra (b) of Li-0.75/NH_2/MIL-101(Cr) after adsorption.

Table 8 Comparison of the Li^+ adsorption capacity between Li-0.75/NH_2/MIL-101(Cr) and Li-1.0/NH_2/MIL-100(Fe) and other MOFs adsorbents studied

Adsorbents	*Q*	Ref.
MIL-100(Fe)	48.8 mg g^{-1}	8
TJU-21	41.1 mg g^{-1}	48
WP@PSS@Cu-MOF	9.69 mg g^{-1}	49
MIL-121	0.18 mmol g^{-1}	7
pNCE/MOF-808	0.016 mmol g^{-1}	50
PDMVBA-MIL-121	0.56 mmol g^{-1}	51
LMOF-321	12.18 mg g^{-1}	52
PSP-UiO-66	10.17 mmol g^{-1}	53
MOFs-808-EDTA	4.34 mmol g^{-1}	54
Li-0.75/NH_2/MIL-101(Cr)	43.58 mg g^{-1}	This study
Li-1.0/NH_2/MIL-100(Fe)	35.22 mg g^{-1}	

reported MOFs or MOF-based adsorbents. The results demonstrate that the adsorbents synthesized in this study exhibit competitive adsorption capacities, indicating strong potential for practical applications or further optimization.

3.3 Li^+ separation performance and mechanism

3.3.1 Separation of Li^+ and Mg^{2+}. Simulated solutions with varying Mg^{2+}/Li^+ ratios, with a low Mg^{2+}/Li^+ ratio of 3 and high Mg^{2+}/Li^+ ratios of 10, 50, 100, and 500, respectively, were used as adsorption targets to assess the selective adsorption performance of Li-0.75/MIL-101(Cr), Li-0.5/MIL-100(Fe), Li-0.75/NH_2/MIL-101(Cr) and Li-1.0/NH_2/MIL-100(Fe). The Li^+ adsorption capacities and separation factors are presented in Fig. 19 (a–d). At low Mg^{2+}/Li^+ ratios, where Mg^{2+} concentration is relatively low, Li^+ is preferentially adsorbed. As the Mg^{2+} concentration increases, Mg^{2+} competitive adsorption intensifies, leading to a significant decline in both Li^+ adsorption capacity and separation factors. Notably, Li-0.75/NH_2/MIL-101(Cr) exhibits superior separation efficiency over Li-1.0/NH_2/MIL-100(Fe). The separation coefficients of Li-0.75/MIL-101(Cr) and Li-0.5/MIL-100(Fe) are markedly lower than those of their aminated counterparts, clearly demonstrating that $-NH_2$ modification significantly enhances the separation performance of the adsorbents.

At low Mg^{2+}/Li^+ ratios, both Li-0.75/NH_2/MIL-101(Cr) and Li-1.0/NH_2/MIL-100(Fe) exhibit $\alpha > 80$, demonstrating their strong affinity for Li^+. Mg^{2+} and Li^+ separation primarily relies on electrostatic attraction and coordination competition. The lone pair electrons on the amino N atoms preferentially form weak coordination bonds with Li^+. Although Mg^{2+} has a higher charge density, its significantly greater hydration energy necessitates overcoming a larger energy barrier for desolvation,[55,56] rendering it difficult to penetrate the adsorbent pores or engage in effective coordination. Additionally, the introduction of $LiNO_3$ as a mineralizer during the synthesis process may enable Li^+ to act as a template, creating Li^+-size-adapted microenvironments within the pores that enhance Li^+ recognition capability.

However, as the Mg^{2+} concentration increases, the high concentration gradient drives faster diffusion of Mg^{2+} into the pore channels, where it competes for adsorption sites. When excessive Mg^{2+} enters the pores, aggregation occurs, blocking diffusion pathways. Mg^{2+} may coordinate with negatively charged groups, reducing the availability of Li^+ adsorption sites. Additionally, Mg^{2+} can neutralize the negative charges of the adsorbent's surface through its charge advantage, weakening the electrostatic attraction for Li^+ and even causing localized charge reversal, which triggers desorption of already adsorbed Li^+.[57,58] Although Mg^{2+} has high hydration energy, its hydration shell may partially dissociate when passing through narrow pores under high-concentration conditions, effectively reducing its effective size and enabling entry into

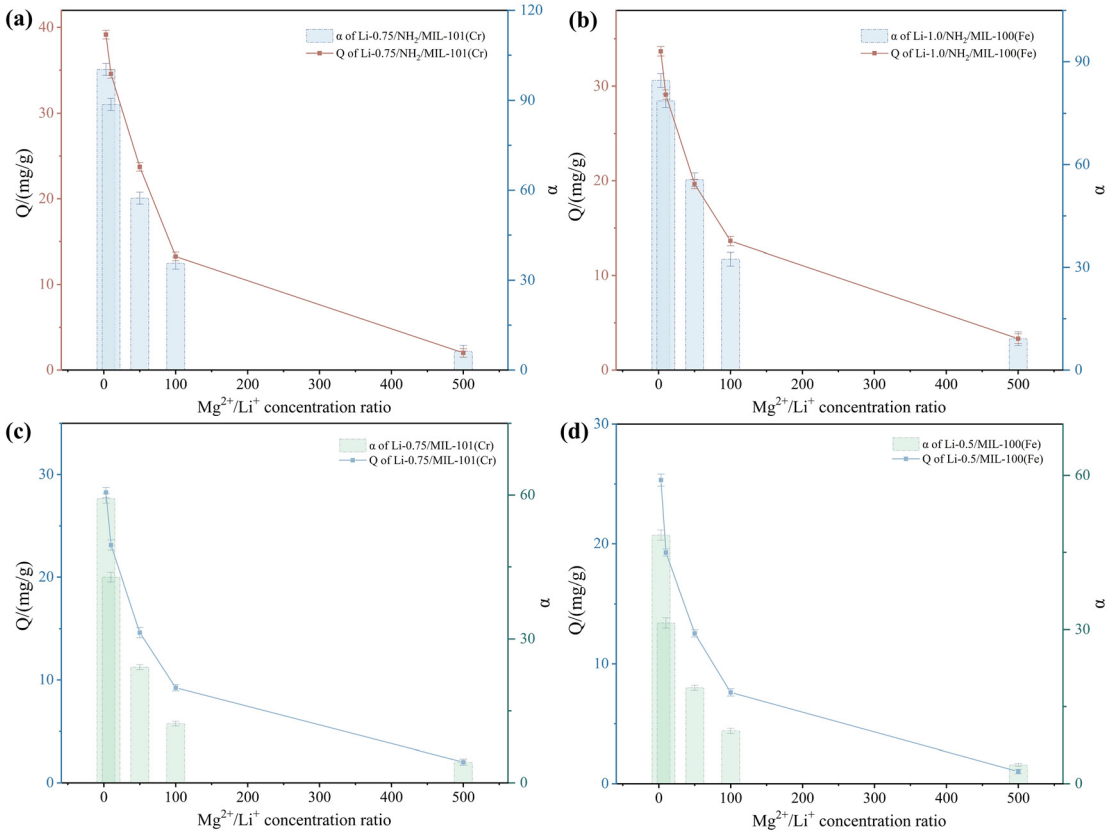

Fig. 19 The Li^+ adsorption capacity and separation factor of Li-0.75/NH_2/MIL-101(Cr) (a), Li-1.0/NH_2/MIL-100(Fe) (b), Li-0.75/MIL-101(Cr) (c) and Li-0.5/MIL-100(Fe) (d).

the adsorbent interior. Furthermore, pre-loaded Li^+ in the synthesis process from $LiNO_3$ may undergo ion-exchange displacement by high-concentration Mg^{2+}, whereby the released Li^+ contributes to an apparent decrease in adsorption capacity. The chemical equation is presented in eqn (11):

$$Li^+\text{-MOF} + Mg^{2+} \rightarrow Mg^{2+}\text{-MOF} + Li^+ \quad (11)$$

Additionally, proton-assisted exchange occurs as shown in eqn (12):

$$Li^+\text{-MOF} + H^+\text{-MOF} + Mg^{2+} \rightarrow Mg^{2+}\text{-MOF} + Li^+ + H^+ \quad (12)$$

In practice, Li-1.0/NH_2/MIL-100(Fe) features smaller window apertures (0.55–0.86 nm), which partially restrict Li^+ diffusion within the channels but induce significant confinement effects. Specifically, the windows only permit Li^+ passage, with the partial hydration shell being dissociated, enabling its access to pore cages and interaction with metal centers *via* coordination or electrostatic forces, while effectively blocking larger hydrated Mg^{2+} through the size-sieving effect. However, the actual separation performance of Li-1.0/NH_2/MIL-100(Fe) is inferior to that of Li-0.75/NH_2/MIL-101(Cr). This discrepancy may arise from: (1) the organic ligand of Li-1.0/NH_2/MIL-100(Fe) is H_3BTC, while the functional ligand is 2-NH_2-BDC, resulting in structural differences that alter window dimensions and framework geometry, potentially weakening size-sieving effects, and additionally, the amination degree of Li-1.0/NH_2/MIL-100(Fe) is lower than that of Li-0.75/NH_2/MIL-101(Cr) due to divergent synthetic protocols; (2) potential Fe–O bond cleavage during amination may deactivate metal sites,[32,59] coupled with Fe^{3+} framework oxidation that deactivates adsorption sites;[60] and (3) Fe^{3+} exhibits weaker coordination capability and electrostatic attraction compared to Cr^{3+}. While Li-0.75/NH_2/MIL-101(Cr) has larger windows,[61,62] the extreme charge density and stable hydration shell of Mg^{2+} preclude it from crossing channels and achieving efficient penetration like Li^+ despite its small ionic radius. Thus, even without optimal size-sieving, Li-0.75/NH_2/MIL-101(Cr) achieves efficient ion-selective adsorption through electrostatic and coordination disparities. Nevertheless, Cr^{3+} sites may strongly coordinate with Mg^{2+},[63] causing more rapid α decay for Li-0.75/NH_2/MIL-101(Cr) under high Mg^{2+}/Li^+ ratios, whereas the narrower pores of Li-1.0/NH_2/MIL-100(Fe) restrict Mg^{2+} diffusion, indirectly preserving Li^+ adsorption sites.[53]

3.3.2 Separation of other interfering ions. In addition to Mg^{2+} and Li^+, other ions such as Na^+, K^+, and Ca^{2+} may also interfere with Li^+ adsorption through competitive binding. Simple binary ion systems (Li–Na, Li–K, and Li–Ca, all with initial ions ratios of 10) and complex multi-ion mixed simulated aqueous systems were used as adsorption targets to

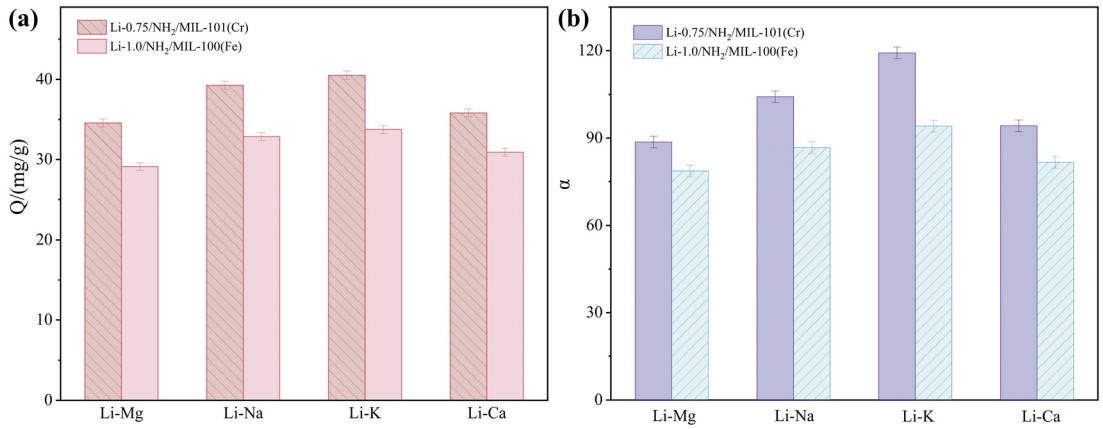

Fig. 20 The Li^+ adsorption capacity (a) and separation factor (b) of Li-0.75/NH_2/MIL-101(Cr) and Li-1.0/NH_2/MIL-100(Fe) in the Li–Mg, Li–Na, Li–K and Li–Ca system.

Table 9 The separation parameters of Li-0.5/UIO-66 and Li-0.75/HKUST-1 in the simulated mixture solvent system

Parameters	Materials	Li^+	Na^+	K^+	Mg^{2+}	Ca^{2+}
Iron concentration (g L^{-1})	Simulated mixture solvent	0.0241	6.5975	0.9012	2.2154	0.0375
Q (mg g^{-1})	Li-0.5/UIO-66	3.68	52.86	2.24	20.13	0.18
	Li-0.75/HKUST-1	3.21	48.17	2.18	19.25	0.17
$\alpha_{Li/M}$	Li-0.5/UIO-66	—	22.31	72.24	19.65	37.36
	Li-0.75/HKUST-1	—	20.90	63.39	17.53	33.75

evaluate the selective adsorption performance of Li-0.75/NH_2/MIL-101(Cr) and Li-1.0/NH_2/MIL-100(Fe). The detailed separation results of simple adsorption systems are illustrated in Fig. 20(a and b).

Consistent with the Li–Mg system, Li-0.75/NH_2/MIL-101(Cr) exhibits superior separation performance compared to Li-1.0/NH_2/MIL-100(Fe) across all tested binary mixed systems. The distribution coefficients follow the order: $Li^+ \gg Mg^{2+} > Ca^{2+} > Na^+ > K^+$. Despite the smaller hydrated radii of Na^+ and K^+ as monovalent ions, their lower charge density and weaker electrostatic interactions result in diminished competitive adsorption. Consequently, both adsorbents maintain effective Li^+ adsorption and separation performance in the presence of monovalent ions. The lower selectivity for divalent ions (*vs.* monovalent ions) arises from a combination of factors, including size sieving, coordination selectivity, charge density disparities, dehydration kinetics, electrostatic interactions, and competitive adsorption.[64,65] Compared to the Li–Mg system, both Li-0.75/NH_2/MIL-101(Cr) and Li-1.0/NH_2/MIL-100(Fe) demonstrate higher Li^+ adsorption capacities and separation factors in the other three binary systems, confirming that Mg^{2+} and Li^+ separation poses the most significant challenge.

The separation parameters of Li-0.75/NH_2/MIL-101(Cr) and Li-1.0/NH_2/MIL-100(Fe) in the complex multi-ionic simulated aqueous system are listed in Table 9. When multiple interfering ions coexist, the adsorbents exhibit significantly reduced Li^+ adsorption capacities and separation factors, yet retain their selective capabilities. This demonstrates that the diverse ions mutually influence adsorption and separation processes. Notably, both adsorbents effectively separate Li^+ from K^+ ($\alpha > 50$) and maintain selectivity toward Na^+ even when the Na^+ concentration is several-fold higher than that of other ions.

In conclusion, both Li-0.75/NH_2/MIL-101(Cr) and Li-1.0/NH_2/MIL-100(Fe) exhibit selective adsorption toward Li^+ in simple systems containing Li–Mg, Li–Na, Li–K, and Li–Ca mixtures, demonstrating their practical applicability for lithium separation. Moreover, both materials hold potential for integration with other separation technologies to further enhance their performance in complex environments.

4. Conclusion

For representative MIL-type MOFs, MIL-101(Cr) and MIL-100(Fe), aminated modifications were performed while introducing $LiNO_3$ as both a mineralizer and a template during synthesis, yielding functionalized adsorbents Li/NH_2/MIL-101(Cr) and Li/NH_2/MIL-100(Fe). The Li^+ adsorption capacities of these adsorbents are influenced by $LiNO_3$ dosage, initial Li^+ concentration, temperature, adsorbent dosage, and pH, with maximum capacities reaching 43.58 and 38.22 mg g^{-1}, respectively. In addition, based on the establishment of kinetic and thermodynamic models, it is concluded that the materials undergo monolayer chemical adsorption, and the adsorption process is exothermic. Compared with Li-1.0/NH_2/MIL-100(Fe), Li/NH_2/MIL-101(Cr) exhibits superior reusability, retaining

over 90% of its initial adsorption capacity after four cycles, while Li-1.0/NH_2/MIL-100(Fe) can still maintain more than 85% of its adsorption capacity after four cycles of adsorption. In binary mixed systems (Li–Mg, Li–K, Li–Na, and Li–Ca), the adsorbents exhibit excellent selective adsorption toward Li^+. At low Mg^{2+}/Li^+ ratios, both Li-0.75/NH_2/MIL-101 (Cr) and Li-1.0/NH_2/MIL-100 (Fe) exhibit an α value greater than 80. When the Mg^{2+}/Li^+ ratio is less than 100, the α value still exceeds 30. Although separation efficiency decreases in multi-ion mixed systems, the selectivity is certainly retained, suggesting potential for integration with other separation processes to optimize the performance. In summary, Li/NH_2/MIL-101(Cr) and Li/NH_2/MIL-100(Fe) serve as effective adsorbents for Li^+ extraction from liquid lithium resources.

Author contributions

Y. J. Zhou put forward the concept, designed the experiments, and wrote the original draft. Y. J. Zhou, X. D. Tang and J. J. Li developed the detailed experimental methodology and data analysis. X. D. Tang designed and supervised the experiments. J. J. Li and D. Y. Qing reviewed and edited the manuscript. D. Y. Qing and H. Wang performed the experiments. All the authors discussed the results and commented on the manuscript.

Conflicts of interest

The authors declare no competing financial interests.

Data availability

All data generated or analyzed during this study are included in this published.

References

1 H. Zhang, X. Hu, T. Li, *et al.*, MIL series of metal organic frameworks (MOFs) as novel adsorbents for heavy metals in water: A review, *J. Hazard. Mater.*, 2022, **429**, 128271.
2 I. H. Alsohaimi, A highly permeable Al-based MOF-sulfonated polyaniline/polyethersulfone composite UF membrane with prominent antifouling properties, *Sep. Purif. Technol.*, 2025, **357**(PartB), 130240.
3 H. M. A. Hassan, M. S. Alruwaili, I. H. Alsohaimi, *et al.*, Electrospun polyacrylonitrile nanofiber composites integrated with Al-MOF/mesoporous carbon for superior CO_2 capture and VOC removal, *Diamond Relat. Mater.*, 2024, **149**, 111649.
4 T. M. McDonald, J. A. Mason, V. Crocella, *et al.*, Cooperative insertion of CO_2 in diamine-appended metal–organic frameworks, *Nature*, 2015, **519**(7543), 303–308.
5 S. Fan, X. Lu, H. Li, *et al.*, Efficient removal of organophosphate esters by ligand functionalized MIL-101 (Fe): Modulated adsorption and DFT calculations, *Chemosphere*, 2022, **302**, 134881.
6 J. Li, L. Liang, H. Zhou, *et al.*, Molecular dynamics simulation study of drugs adsorption in UiO–66, *Z. Anorg. Allg. Chem.*, 2022, **649**(1), 261.
7 Q. Wei, B. Shi, F. Wang, *et al.*, Simple and rapid preparation of MIL-121 with small particles for lithium adsorption from brine, *Coatings*, 2021, **11**(7), 237643006.
8 C. Huangfu, S. Yu, B. Tong, *et al.*, Efficient lithium extraction from aqueous solutions by MIL-100(Fe): A study on adsorption kinetics, thermodynamics and mechanism, *Sep. Purif. Technol.*, 2023, **322**, 124365.
9 X. Guo, H. Xu, Y. Tang, *et al.*, Confining iodine into metal–organic framework derived metal–nitrogen–carbon for long–life aqueous zinc–iodine batteries, *Adv. Mater.*, 2024, **36**(38), 2408317.
10 Y. Shi, G. Song, B. Yang, *et al.*, Prussian Blue analogues "dressed" in MXene nanosheets tightly for high performance lithium-ion batteries, *Adv. Mater.*, 2025, **37**(8), 2416665.
11 Y. J. Zhou, X. D. Tang, D. Y. Qing, *et al.*, Research progress of technology of lithium extraction, *Sep. Purif. Technol.*, 2025, **359**, 130561.
12 P. Horcajada, S. Surble, C. Serre, *et al.*, Synthesis and catalytic properties of MIL-100(Fe), an iron(III) carboxylate with large pores, *Chem. Commun.*, 2007, **27**(27), 2820–2822.
13 F. F. Liu, J. Zhao, S. Wang, *et al.*, Effects of solution chemistry on adsorption of selected pharmaceuticals and personal care products (PPCPs) by graphenes and carbon nanotubes, *Environ. Sci. Technol.*, 2014, **48**(22), 13197–13206.
14 K. J. Yao, M. Wen and S. Zhou, Synthesis and water absorbency of the copolymer of acrylamide with anionic monomers, *J. Appl. Polym. Sci.*, 2010, **53**(11), 1533–1538.
15 Y. S. Ho and G. Mckay, A kinetic study of dye sorption by biosorbent waste product pith, *Resour., Conserv. Recycl.*, 1999, **25**(3–4), 171–193.
16 H. Schott, Swelling kinetics of polymers, *J. Macromol. Sci., Part B: Phys.*, 2006, **31**(1), 1–9.
17 D. Cabooter, H. Song, D. Makey, *et al.*, Measurement and modelling of the intra-particle diffusion and b-term in reversed-phase liquid chromatography, *J. Chromatogr. A*, 2021, **1637**, 461852.
18 H. Tun and C. C. Chen, Isosteric heat of adsorption from thermodynamic Langmuir isotherm, *Adsorption*, 2021, **27**(6), 979–989.
19 E. Glueckauf, Theory of chromatography; separation of two solutes following a Freundlich isotherm, *J. Chem. Soc.*, 1947, 1321–1329.
20 H. N. Tran, S. J. You, B. Hosseini, *et al.*, Mistakes and inconsistencies regarding adsorption of contaminants from aqueous solutions: A critical review, *Water Res.*, 2017, **120**, 88–116.

21 D. Jiang, L. L. Keenan, A. D. Burrows, *et al.*, Synthesis and post-synthetic modification of MIL-101(Cr)-NH_2 via a tandem diazotisation process, *Chem. Commun.*, 2012, **48**(99), 12053–12055.
22 Z. Li, X. Liu, W. Jin, *et al.*, Adsorption behavior of arsenicals on MIL-101(Fe): The role of arsenic chemical structures, *J. Colloid Interface Sci.*, 2019, **554**, 692–704.
23 Z. Noorpoor, S. G. Pakdehi and A. Rashidi, High capacity and energy-efficient dehydration of liquid fuel 2-dimethyl amino ethyl azide (DMAZ) over chromium terephthalic (MIL-101) nanoadsorbent, *Adsorption*, 2017, **23**(5), 743–752.
24 Diercks, Christian S., *et al.*, The role of reticular chemistry in the design of CO_2 reduction catalysts, *Nat. Mater.*, 2018, **17**, 301.
25 S. Marchesini, C. M. McGilvery, J. Bailey, *et al.*, Template-free synthesis of highly porous boron nitride: Insights into pore network design and impact on gas sorption, *ACS Nano*, 2017, **11**(10), 10003–10011.
26 L. Yang, T. Zhao, I. Boldog, *et al.*, Benzoic acid as a selector-modulator in the synthesis of MIL-88B(Cr) and nano-MIL-101(Cr), *Dalton Trans.*, 2019, **48**(3), 989–996.
27 T. Zhao, F. Jeremias, I. Boldog, *et al.*, High-yield, fluoride-free and large-scale synthesis of MIL-101(Cr), *Dalton Trans.*, 2015, **44**(38), 16791–16801.
28 Z. Wei, G. Qiang, W. Yingjun, *et al.*, Synthesis of Pt/PMA-MIL-101 catalyst and its performance in n-heptane isomerization, *China Pet. Process. Petrochem. Technol.*, 2024, **26**(3), 63–72.
29 Z. H. Khan, M. Gao, W. Qiu, *et al.*, Efficient As(III) removal by novel MoS(2)-impregnated Fe-oxide-biochar composites: Characterization and mechanisms, *ACS Omega*, 2020, **5**(22), 13224–13235.
30 S. Liu, J. Wang, W. Huang, *et al.*, Adsorption of phenolic compounds from water by a novel ethylenediamine rosin-based resin: Interaction models and adsorption mechanisms, *Chemosphere*, 2018, **214**, 821–829.
31 S. Kim, J. Hou, N. Choudhury, *et al.*, Electrospun membranes of hydrophobic polyimide and NH2-UiO-66 nanocomposite for desalination, *Energy Environ. Mater.*, 2024, **8**(2), 12841.
32 J. J. Delgado-Marín, J. Narciso, E. V. Ramos-Fernández, *et al.*, Effect of the synthesis conditions of MIL-100(Fe) on its catalytic properties and stability under reaction conditions, *Materials*, 2022, **15**(18), 6499.
33 H. Lee, D. I. Kim, Y. Kim, *et al.*, Efficient one-pot synthesis of magnetic MIL-100(Fe) using nitric acid without additional Fe ion addition and adsorption behavior of charged organic compounds, *Chemosphere*, 2022, **314**, 137696.
34 Y. Luo, B. Tan, X. Liang, *et al.*, Investigation on water vapor adsorption performance of LiCl@MIL0(Fe) composite adsorbent for adsorption heat pumps, *Int. J. Energy Res.*, 2020, **44**(7), 5361.
35 W. Li, T. Zhang, L. Lv, *et al.*, Room-temperature synthesis of MIL-100(Fe) and its adsorption performance for fluoride removal from water, *Colloids Surf., A*, 2021, **624**, 126791.
36 S. Wang, S. Hou, C. Wu, *et al.*, $RuCl_3$ anchored onto post-synthetic modification MIL-101(Cr)-NH2 as heterogeneous catalyst for hydrogenation of CO_2 to formic acid, *Chin. Chem. Lett.*, 2019, **5**(2), 398–402.
37 Y. Ren, Y. Yin, J. Y. Zhang, *et al.*, Trade-off between Fenton-like activity and structural stability of MILs(Fe), *Chem. Eng. J.*, 2021, **420**(15), 129583.
38 N. A. Elessawy, M. Elnouby, M. H. Gouda, *et al.*, Ciprofloxacin removal using magnetic fullerene nanocomposite obtained from sustainable PET bottle wastes: Adsorption process optimization, kinetics, isotherm, regeneration and recycling studies, *Chemosphere*, 2020, **239**, 124728.
39 D. C. Mei, L. J. Liu and B. Yan, Adsorption of uranium(VI) by metal–organic frameworks and covalent–organic frameworks from water, *Coord. Chem. Rev.*, 2023, **475**, 15.
40 J. Du, J. Ren, M. Shu, *et al.*, Insights into the capacity and rate performance of transition-metal coordination compounds for reversible lithium storage, *Angew. Chem., Int. Ed.*, 2021, **60**(8), 4142–4149.
41 C. I. Ezugwu, S. Zhang, S. Li, *et al.*, Efficient transformative HCHO capture by defective NH_2-UiO-66(Zr) at room temperature, *Environ. Sci.: Nano*, 2019, **6**(10), 2931–2936.
42 M. K. Alsaedi, G. K. Alothman, M. N. Alnajrani, *et al.*, Antibiotic adsorption by metal–organic framework (UiO-66): A comprehensive kinetic, thermodynamic, and mechanistic study, *Antibiotics*, 2020, **9**(10), 722.
43 G. Chen, S. He, G. Shi, *et al.*, *In situ* immobilization of ZIF-67 on wood aerogel for effective removal of tetracycline from water, *Chem. Eng. J.*, 2021, **423**, 130184.
44 Y. Sun, J. L. Chen, A. M. Li, *et al.*, Adsorption of phenol from aqueous solution by aminated hypercrosslinked polymers, *Adsorpt. Sci. Technol.*, 2005, **23**(4), 335–346.
45 Z. Zhang, Y. Chen, P. Wang, *et al.*, Facile fabrication of N-doped hierarchical porous carbons derived from soft-templated ZIF-8 for enhanced adsorptive removal of tetracycline hydrochloride from water, *J. Hazard. Mater.*, 2022, **423**(Pt B), 127103.
46 A. Khutia, H. U. Rammelberg, T. Schmidt, *et al.*, Water sorption cycle measurements on functionalized MIL-101Cr for heat transformation application, *Chem. Mater.*, 2013, **25**(5), 790–798.
47 G. Ferey, C. Mellot-Draznieks, C. Serre, *et al.*, A chromium terephthalate-based solid with unusually large pore volumes and surface area, *Science*, 2005, **309**(5743), 2040–2042.
48 X. Jiang, B. Wu, P. Bai, *et al.*, Novel fluorine-pillared metal–organic framework for highly effective lithium enrichment from brine, *ACS Appl. Mater. Interfaces*, 2021, **13**(40), 47793–47799.
49 W. Bian, J. Chen, Y. Chen, *et al.*, A novel waste paper cellulose-based Cu-MOF hybrid material threaded by PSS for lithium extraction with high adsorption capacity and selectivity, *Cellulose*, 2021, **28**(5), 3041–3054.
50 S. Zhang, R. Ou, H. Ma, *et al.*, Thermally regenerable metal–organic framework with high monovalent metal ion selectivity, *Chem. Eng. J.*, 2021, **405**, 127037.

51 R. Ou, H. Zhang, J. Wei, *et al.*, Thermoresponsive amphoteric metal–organic frameworks for efficient and reversible adsorption of multiple salts from water, *Adv. Mater.*, 2018, **30**(34), 1802767.
52 N. D. Rudd, Y. Liu, K. Tan, *et al.*, Luminescent metal–organic framework for lithium harvesting applications, *ACS Sustainable Chem. Eng.*, 2019, **7**(7), 6561–6568.
53 X. Wu, H. Zhang, X. Zhang, *et al.*, Sustainable lithium extraction enabled by responsive metal–organic frameworks with ion-sieving adsorption effects, *Proc. Natl. Acad. Sci. U. S. A.*, 2024, **121**(6), e2309852121.
54 C. Ji, H. Yu, J. Lu, *et al.*, High-efficiency and sustainable desalination using thermo-regenerable MOF-808-EDTA: Temperature-regulated proton transfer, *ACS Appl. Mater. Interfaces*, 2021, **13**(20), 23833–23842.
55 G. Han, K. M. Rodriguez, Q. Qian, *et al.*, Acid-modulated synthesis of high surface area amine-functionalized MIL-101(Cr) nanoparticles for CO_2 separations, *Ind. Eng. Chem. Res.*, 2020, **59**(40), 18139–18150.
56 Y. Jia, J. Qian and B. Pan, Dual-functionalized MIL-101(Cr) for the selective enrichment and ultrasensitive analysis of trace per- and poly-fluoroalkyl substances, *Anal. Chem.*, 2021, **93**(32), 11116–11122.
57 D. L. S. J. Banerjee, Synthesis and structural characterization of lithium-based metal–organic frameworks, *Cryst. Growth Des.*, 2009, **9**(11), 4922–4926.
58 R. Wang, M. Fu, J. Yang, *et al.*, Surface charge regulation of MIL-100(Fe) by anion exchange for demulsifying the cationic surfactant-stabilized O/W emulsion, *ACS Appl. Mater. Interfaces*, 2021, **13**(42), 49964–49973.
59 S. Wang, Y. Fang, W. Han, *et al.*, MOF-derived hollow spheres of MIL-100(Fe)-NH(2)(20) with well-developed hierarchical mesoporous and uniform distribution of Fe and N active phases for the photocatalytic removal of organic dyes, *Langmuir*, 2023, **39**(26), 9130–9143.
60 S. Fan, X. Lu, H. Li, *et al.*, Efficient removal of organophosphate esters by ligand functionalized MIL-101 (Fe): Modulated adsorption and DFT calculations, *Chemosphere*, 2022, **302**, 134881.
61 S. Zhang, J. Ding, D. Tian, *et al.*, Adsorption behavior and mechanism of NH_2-MIL-101(Cr)@COFs@SA composite adsorbent for tetracycline removal, *Polymer*, 2024, **312**, 127631.
62 O. I. Lebedev, F. Millange, C. Serre, *et al.*, First direct imaging of giant pores of the metal–organic framework MIL-101, *Chem. Mater.*, 2005, **17**, 26.
63 K. Liu, S. Zhang, X. Hu, *et al.*, Understanding the adsorption of PFOA on MIL-101(Cr)-based anionic-exchange metal–organic frameworks: Comparing DFT calculations with aqueous sorption experiments, *Environ. Sci. Technol.*, 2015, **49**(14), 8657–8665.
64 D. Bahamon, W. Anlu, S. Builes, *et al.*, Effect of amine functionalization of MOF adsorbents for enhanced CO_2 capture and separation: A molecular simulation study, *Front. Chem.*, 2021, **8**, 574622.
65 S. Dhir, B. Jagger, A. Maguire, *et al.*, Fundamental investigations on the ionic transport and thermodynamic properties of non-aqueous potassium-ion electrolytes, *Nat. Commun.*, 2023, **14**(1), 3833.

